CM²

MAGAZINE

第 44 期

创刊词

海洋是生命的摇篮，是文明的纽带。地球上最早的生命诞生于海洋，海洋里的生命最终进化成了人类，人类的文化融合又通过海洋得以实现。人因海而兴。

人类对海洋的探索从未停止。从远古时代美丽的神话传说，到麦哲伦的全球航行，再到现代对大洋的科学钻探计划，海洋逐渐从人类敬畏崇拜幻想的精神寄托演变成可以开发利用与科学研究的客观存在。其中，上个世纪与太空探索同步发展的大洋科学钻探计划将人类对海洋的认知推向了崭新的纬度：深海（deep sea）与深时（deep time）。大洋钻探计划让人类知道，奔流不息的大海之下，埋藏的却是亿万年的地球历史。它们记录了地球板块的运动，从而使板块构造学说得到证实；它们记录了地球环境的演变，从而让古海洋学方兴未艾。

在探索海洋的悠久历史中，从大航海时代的导航，到大洋钻探计划中不可或缺的磁性地层学，磁学发挥了不可替代的作用。这不是偶然，因为从微观到宏观，磁性是最基本的物理属性之一，可以说，万物皆有磁性。基于课题组的学科背景和对海洋的理解，我们对海洋的探索以磁学为主要手段，海洋磁学中心因此而生。

海洋磁学中心，简称 CM^2，一为其全名 "Centre for Marine Magnetism" 的缩写，另者恰与爱因斯坦著名的质能方程 $E = MC^2$ 对称，借以表达我们对科学巨匠的敬仰和对科学的不懈追求。

然而科学从来不是单打独斗的产物。我们以磁学为研究海洋的主攻利器，但绝不仅限于磁学。凡与磁学相关的领域均是我们关注的重点。为了跟踪反映国内外地球科学特别是与磁学有关的地球科学领域的最新研究进展，海洋磁学中心特地主办 CM^2 Magazine，以期与各位地球科学工作者相互交流学习、合作共进！

"海洋孕育了生命，联通了世界，促进了发展"。21 世纪是海洋科学的时代，由陆向海，让我们携手迈进中国海洋科学的黄金时代

目 录

岩石磁学演绎

第 34 章　磁性参数比值与相关图总结

在磁性矿物种类固定的情况下，磁化率、ARM 和 SIRM 等参数主要受控于磁性矿物的含量与粒径分布。于是，我们可以采用参数比值来压抑含量的影响，突出粒径变化信息。

这类比如包括χ/χ_{ARM}（或者χ_{ARM}/χ）、$\chi/SIRM$、ARM/SIRM、M_{rs}/M_s、χ_{fd}/χ_{ARM}、χ/M_s 等等。

基于χ和 ARM（或χ_{ARM}）与粒径之间的不同行为，Banerjee et al. [1981] 提出建立χ和χ_{ARM}图（the Banerjee diagram）可以有效地检测粒径的变化。King et al. [1982] 通过对比χ_{ARM}与χ_{ferri}修正了 Banerjee diagram，后来被称作 King diagram。
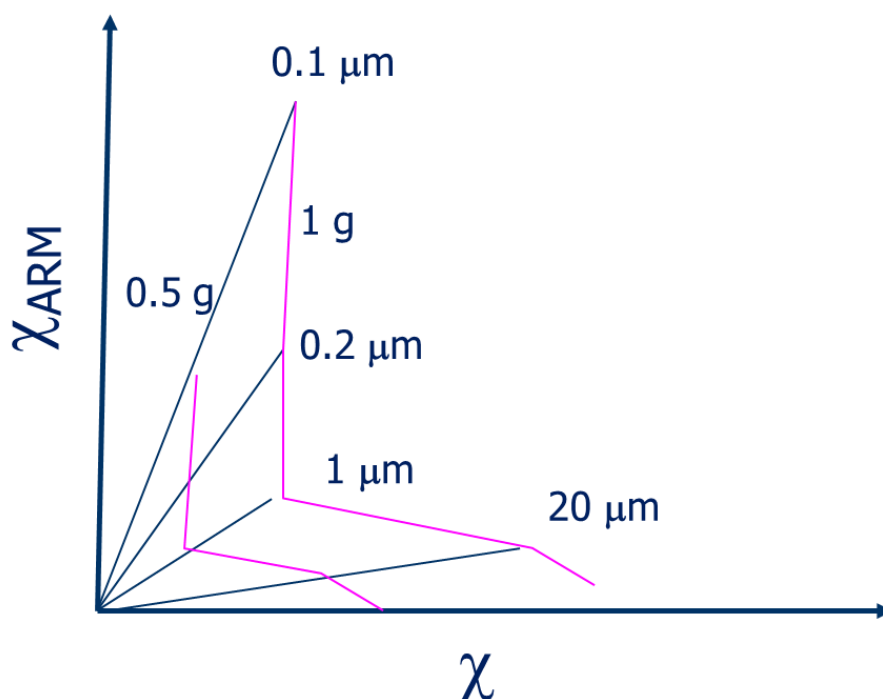

图 1 磁化率和非磁滞剩磁磁化率相关图（King 图）

King 图最大的优势在于可以清晰地判断粒径和含量的双重变化。远离原点，表示含量增加，而向左上方偏转，表示粒径变小。

Kissel et al. (2009)研究了北大西洋钻孔的磁性特征，顺着洋流路径从北向南，会发现两个重要特征，第一个是磁性矿物含量变低，第二个是在 King 图中逐渐向左上方偏转，表示磁性颗粒的粒径逐渐变小。这两个特征符合物理 Sorting 的过程。也就是沿着洋流路径向前，大颗粒会优先沉积，小颗粒会被洋流带往更远处。
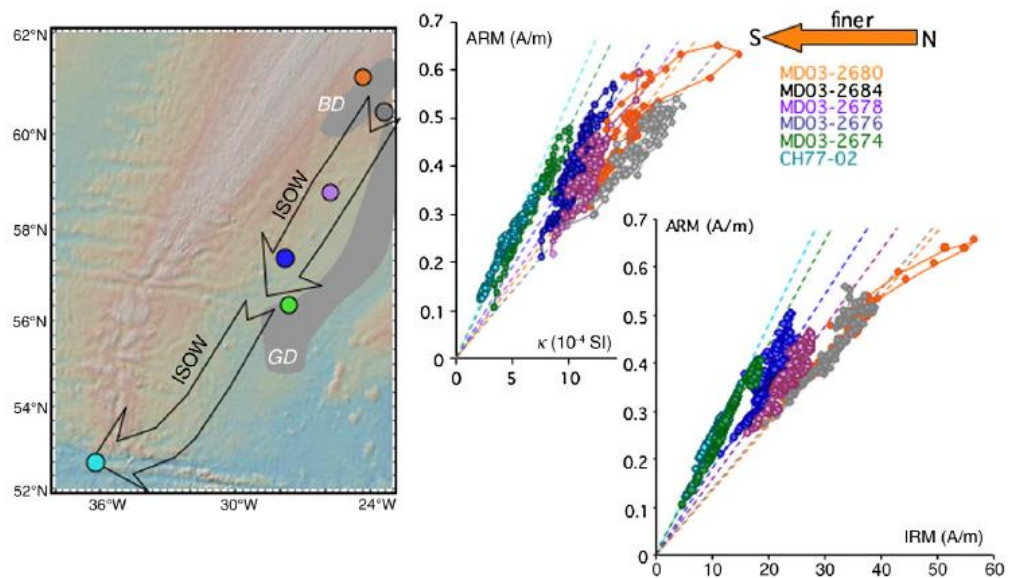

图 2 ARM 与磁化率以及 ARM 与 SIRM 的相关图。采样点在北大西洋（Kissel et al., 2009）

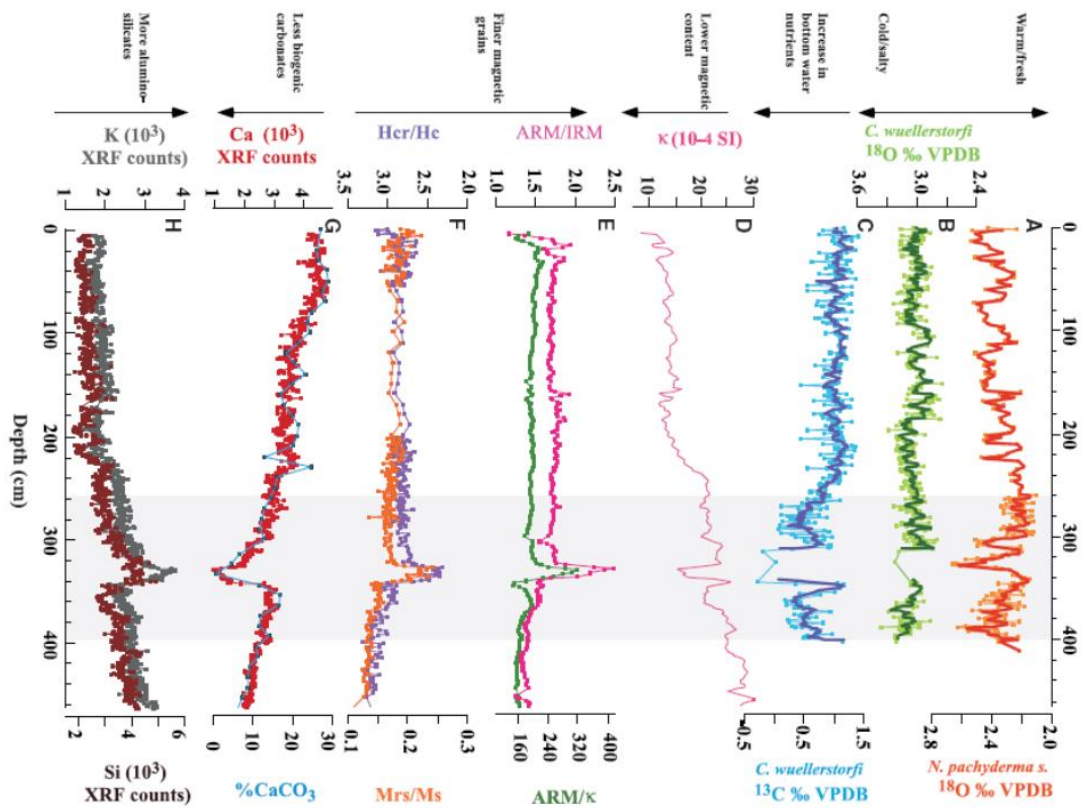在 King 图中任意一点的斜率其实就是χ_{ARM}/χ。于是，我们还可以画 χ_{ARM}/χ 随着深度的变化曲线，进而判断磁性颗粒粒径的大小。

图 3 北大西洋记录的 8.2 ka 冷事件（Kleiven et al., Science, 2008）

在全新世 8.2 ka 发生了一次温度快速降低的冷事件。为了确定这次气候冷事件的机制，Kleiven et al.（2008）研究了该孔的 ARM/k 的变化特征，发现在 8.2 ka 的时候，ARM/k 快速增加，指示磁性颗粒的粒径变小，从而大西洋深层水的洋流流动速度减慢。可见，巧妙地运用磁学参数，可以有效地识别相关的气候和环境问题。
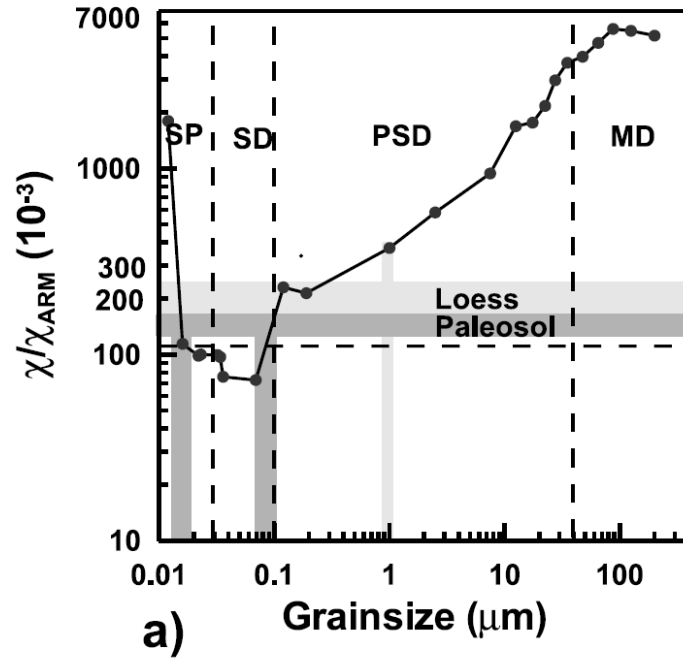
图 4 χ/χ_{ARM} 随着粒径变化图（Liu et al., 2004）

ARM/SIRM 是另外一个常用的粒径变化指标。因为分子和分母都是剩磁，所以顺磁性和超顺磁性颗粒对其没有影响，它主要指示 SD-MD 颗粒的粒径变化。与前面两个参数相比，χ/M_s 应用得并不是很广泛，这主要是因为 M_s 相对不容易获得。这个参数主要突出的是 SP 颗粒的贡献，效果和频率磁化率类似，很多情况下，二者正相关。χ_{fd}/χ_{ARM} 这个比值在土壤等和纳米颗粒密切相关的环境研究中大有作为。我们还经常做二者的相关图。如果测量点都落在一条直线上，就说明 SD-MD 范围，粒径变化不大。如果不落在一条直线上，说明纳米颗粒的粒径发生了变化，是很好的环境指示指标。

综上所述，对于相关图，测量数据如果可以拟合成一条直线，一般都说明粒径很稳定，变化不大。当这条直线过原点时，参数比值与直线斜率相等。但是当存在 X 轴和 Y 轴的截距时，参数比值就会造成错误解释，这种情况一定要加以正视。

我们以 χ_{fd}/χ_{lf} 为例，分子 χ_{fd} 代表着 VSP 颗粒含量的变化，而分母则比较复杂。对于古土壤样品，它包含两部分，一部分是粉尘物质携带的磁化率，和成土无关，也不具有频率磁化率特征。另外一部分是成土产生的纳米颗粒造成的磁化率。如果我们做 $\chi_{lf}\sim\chi_{fd}$ 的相关图，就会发现二者成正相关，可以拟合成一条直线，这充

分说明成土作用产生的纳米颗粒粒径分布很稳定。

当把拟合的直线外延，当$\chi_{fd} = 0$时，也就是说没有成土作用时，所对应的磁化率就认为是粉尘物质最初的磁化率本底值，我们把它记做χ_0。χ_0的变化可以被用来研究物源输入的变化。

文献速递

1. 高纬度生物群落和岩石风化作用调控着偏心率时间尺度上气候-碳循环反馈机制

翻译人：仲义 zhongy@sustech.edu.cn

摘要：国际大洋钻探计划及其前期计划已经产生了关于新生代气候和碳循环动力学过程的宝库。然而，在不断变化的地质气候边界上，气候和碳循环过程仍然不清楚。本文作者总结了大型海洋生物的碳同位素（$\delta^{13}C$）来记录深海 35 Ma 以来 $\delta^{13}C$ 的演化过程。作者将大型海洋生物 $\delta^{13}C$ 及其对应的 $\delta^{18}O$ 进行对比，来确定他们在 100 kyr 偏心率周期上的相位差别。分析表明在 34-6 Ma 之间 2.4-Myr 偏心率周期调控着 $\delta^{13}C$-$\delta^{18}O$ 之间的相位关系。在 6 Ma 开始，一个明显的从同相位到反相位的转换出现，表明全球气候-碳循环系统发生重组。在 6 Ma 以前，主要是以轨道周期调控下变冷时期，表现为低纬度大陆碳库的不断扩张；而在 6 Ma 以后，由于北极生物群落之间的竞争效应，大陆碳库在寒冷时期开始缩减而非扩张。作者认为在地质时间尺度上，地球系统经历了气候-碳循环相互作用的依赖模式。

ABSTRACT: The International Ocean Discovery Programme (IODP) and its predecessors generated a treasure trove of Cenozoic climate and carbon cycle dynamics. Yet, it remains unclear how climate and carbon cycle interacted under changing geologic boundary conditions. Here, we present the carbon isotope ($\delta^{13}C$) megasplice, documenting deep-ocean $\delta^{13}C$ evolution since 35 million years ago (Ma). We juxtapose the $\delta^{13}C$ megasplice with its $\delta^{18}O$ counterpart and determine their phase-difference on ~100-kyr eccentricity timescales. This analysis reveals that 2.4-Myr eccentricity cycles modulate the $\delta^{13}C$-$\delta^{18}O$ phase relationship throughout the Oligo-Miocene (34-6 Ma), potentially through changes in continental weathering. At 6 Ma, a striking switch from in-phase to anti-phase behaviour occurs, signalling a reorganization of the climate-carbon cycle system. We hypothesize that this transition is consistent with Arctic cooling: Prior to 6 Ma, low-latitude

continental carbon reservoirs expanded during astronomically-forced cool spells. After 6 Ma, however, continental carbon reservoirs contract rather than expand during cold periods due to competing effects between Arctic biomes (ice, tundra, taiga). We conclude that, on geologic timescales, System Earth experienced state-dependent modes of climate–carbon cycle interaction.
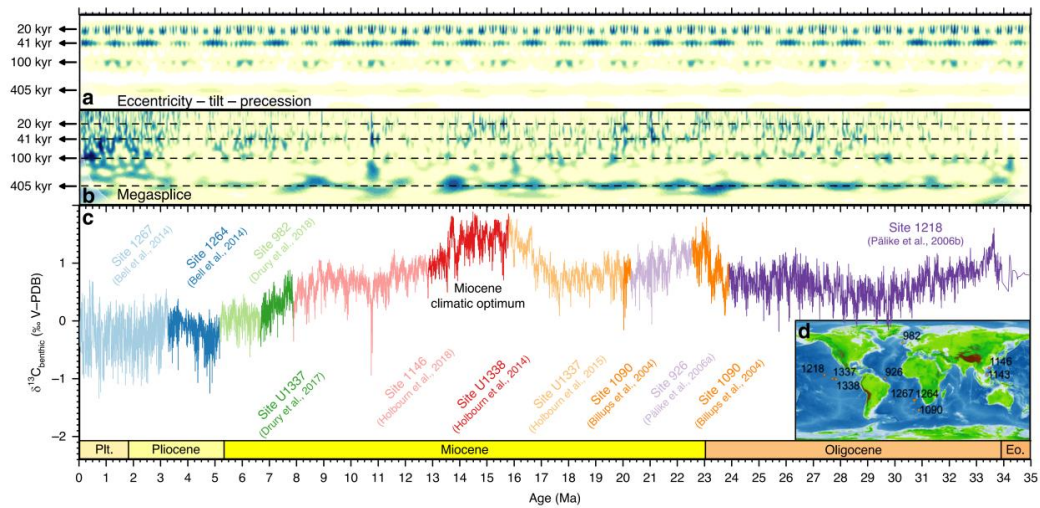

Figure 1. Benthic δ^{13}C megasplice. Wavelet spectrograms of a the astronomical rhythms (eccentricity–tilt–precession[58] composite) and b the benthic δ^{13}C megasplice visualize the strong response of carbon cycle dynamics to 405-kyr long eccentricity. c, d The megasplice consists of nine globally distributed benthic carbon isotope records, all retrieved by the IODP and its predecessors: Site 926[75], 982[19,76], 1090[77], 1146[7,21], 1218[10], 1264[18], 1267[18], U1337[20,70] and U1338[78]. World map after Amante and Eakins[79].
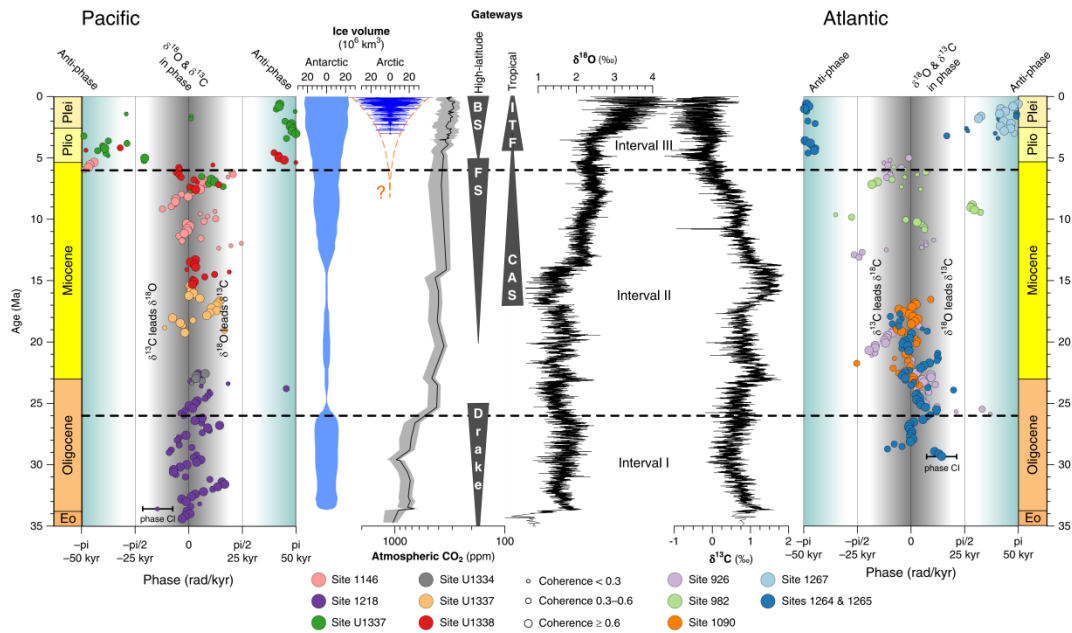
Figure 2. Phase-relationship between $\delta^{13}C$ and $\delta^{18}O$ on 100-kyr eccentricity time-scales. On eccentricity time-scales, $\delta^{13}C$ and $\delta^{18}O$ exhibit cyclic in-phase behaviour from 35 till ~6 Ma in the Pacific, as well as in the Atlantic Ocean (Intervals I and II). Around 6 Ma in the Pacific (Interval III), and somewhat later in the Atlantic, we observe an abrupt shift from in-phase to anti-phase behaviour. The plotted uncertainty bar indicates a typical confidence interval (CI) on the phase estimate of ±0.44 rad. Uncertainty on the phase difference between $\delta^{13}C$ and $\delta^{18}O$ is inversely proportional to coherence and overall ranges between ±0.25 and ±0.59 rad. Antarctic and Arctic ice volume reconstructions are from Oerlemans63 and Berger et al. 80, respectively. The earlier onset of NH glaciation suggested by this study is indicated in red. Atmospheric CO_2 reconstruction from Zhang et al. 81. Grey triangles indicate opening and closing of important ocean gateways. BS, Bering Strait; FS, Fram Strait; Drake, Drake Passage; CAS, Central American Seaway; ITF, Indonesian Throughflow. All Sites that constitute the δ13C megasplice are included here (references in Fig. 1) and are complemented by additional orbital-resolution benthic isotope data from Sites 92682, 98283, 1264/126515,49, U133450,84, U133717 and U13386,85 (data as time-series in Supplementary Fig. 3).
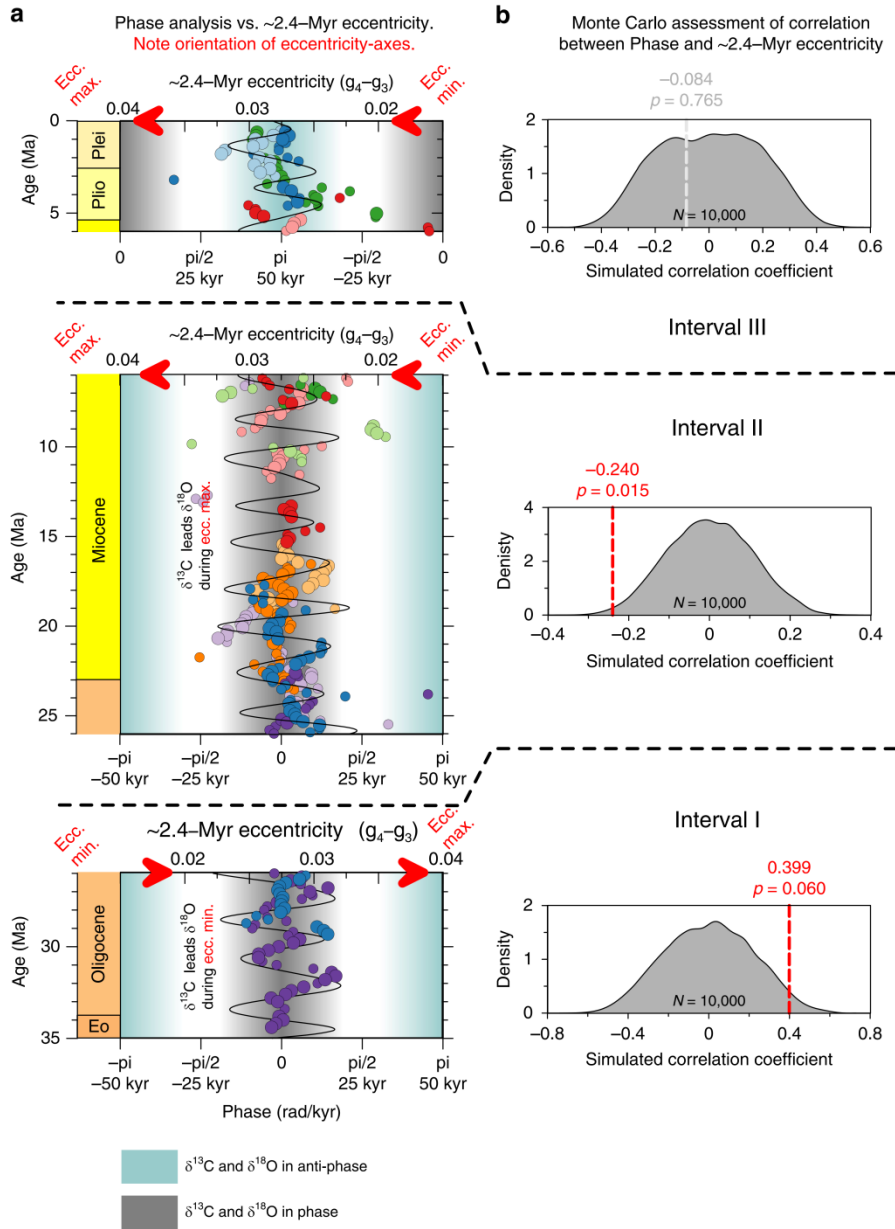
Figure 3. Long 2.4-Myr eccentricity (g4-g3) modulates Oligocene and Miocene leads and lags between $\delta^{13}C$ and $\delta^{18}O$ on 100-kyr eccentricity timescales. a Visual comparison of phase analysis results and 2.4-Myr eccentricity cycles, only considering phase-results with coherence >0.3 (see Fig. 2). b Prior to 26 Ma (Interval I), long 2.4-Myr eccentricity minima correlate with time-intervals when $\delta^{13}C$ leads $\delta^{18}O$ (positive Spearman correlation coefficient of 0.399 between phase and eccentricity). Between 26 and 6 Ma (Interval II), long 2.4-Myr eccentricity minima correlate with time intervals when $\delta^{18}O$ leads $\delta^{13}C$ (negative Spearman correlation coefficient of -0.240). After 6 Ma (Interval III), the correlation between 2.4-Myr eccentricity and phase ceases (R = -0.084).
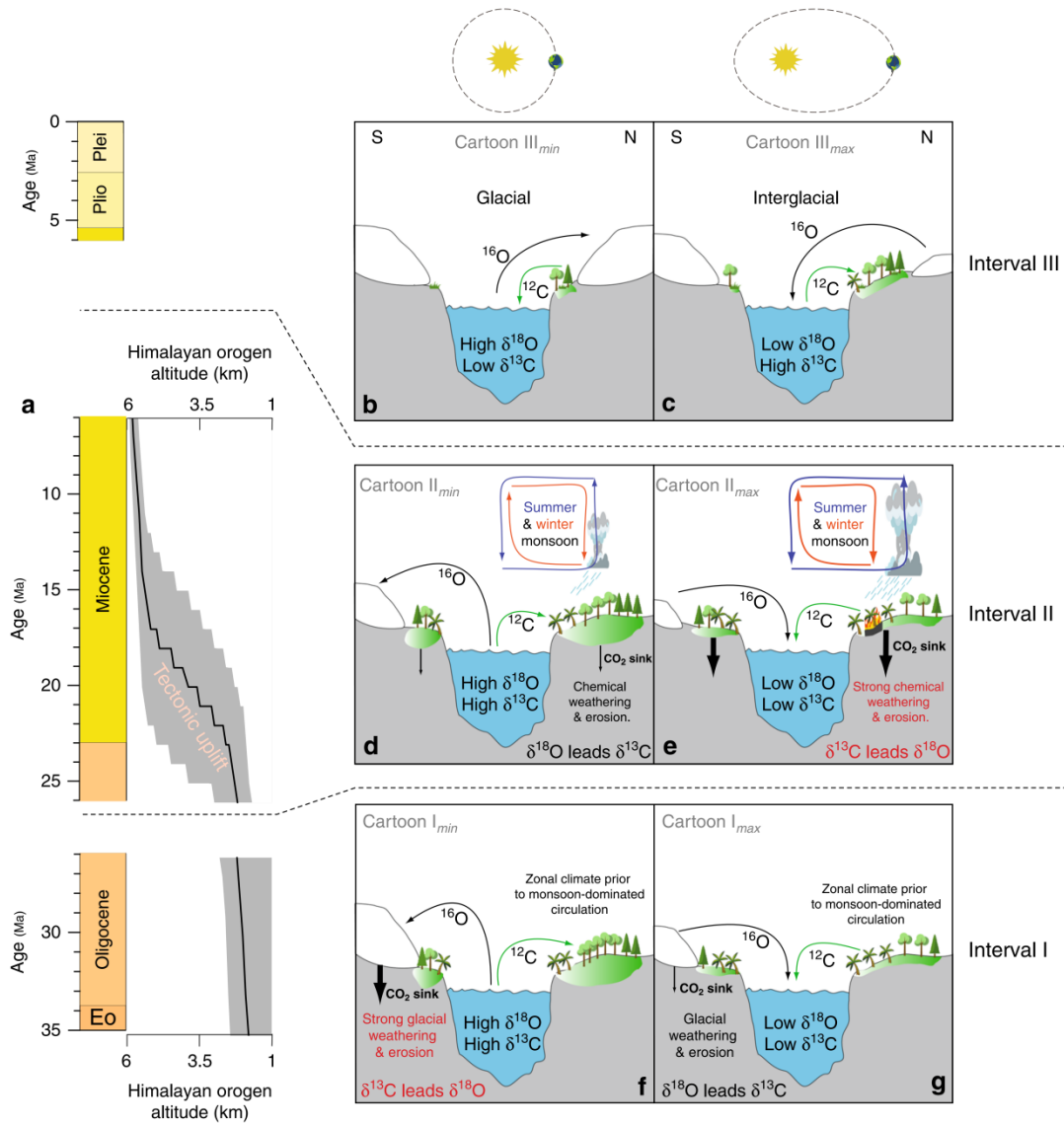
Figure 4. Cartoons illustrating the proposed concepts for the observed phasing patterns between $\delta^{13}C$ and $\delta^{18}O$. a Geologic time-scale of the last 35 Ma, and evolution of the Himalayan Orogen (after Ding et al.[64]). b, c The anti-phase behaviour in Interval III is primarily ascribed to high-latitude biome dynamics. D-g During Intervals I and II, when in-phase behaviour is observed, continental rock weathering forms the key mechanism in our hypotheses, with the carbon cycle ($\delta^{13}C$) leading the climate–cryosphere system ($\delta^{18}O$) when the continental rock weathering CO_2 sink is enhanced. This occurs during eccentricity minima (strong glacial activity) during Interval I, but during eccentricity maxima (strong monsoonal circulation) during Interval II.

2. 亚洲人类活动产生气溶胶为北太平洋提供铁源

翻译人：蒋晓东 jiangxd@sustech.edu.cn

摘要：化石燃料释放生物获得性铁且通过大气气溶胶传输可能影响远洋浮游初级生产力和碳循环。然而这一路径并未被实测观察所证实。本文对北太平洋海域 (158°W，25°N - 42°N)进行高分辨率的微量元素与同位素分析。溶解态铁含量在 35°N 附近出现最大值，这与溶解态铅及铅同位素分布一致，而这铅同位素特征与亚洲工业释放的气溶胶一致。人类活动释放铁同位素具有较低值 (-0.23‰ > δ^{56}Fe > -0.65‰)，原位海水铁同位素分析揭示该区海水铁同位素具有这一特征，表明该区受气溶胶沉降影响。同位素质量平衡分析表明，在北太平洋 35°N - 42°N 区域人类活动产生的铁对海水溶解态铁的贡献在 21-59%。因此人类活动气溶胶铁源很可能是北太平洋铁输入的重要来源。

ABSTRACT: Fossil-fuel emissions may impact phytoplankton primary productivity and carbon cycling by supplying bioavailable Fe to remote areas of the ocean via atmospheric aerosols. However, this pathway has not been confirmed by field observations of anthropogenic Fe in seawater. Here we present high-resolution trace-metal concentrations across the North Pacific Ocean (158°W from 25° to 42°N). A dissolved Fe maximum was observed around 35°N, coincident with high dissolved Pb and Pb isotope ratios matching Asian industrial sources and confirming recent aerosol deposition. Ironstable isotopes reveal in situ evidence of anthropogenic Fe in seawater, with low δ^{56}Fe ($-0.23‰ > \delta^{56}$Fe $> -0.65‰$) observed in the region that is most influenced by aerosol deposition. An isotope mass balance suggests that anthropogenic Fe contributes 21–59% of dissolved Fe measured between 35° and 40°N. Thus, anthropogenic aerosol Fe is likely to be an important Fe source to the North Pacific Ocean.
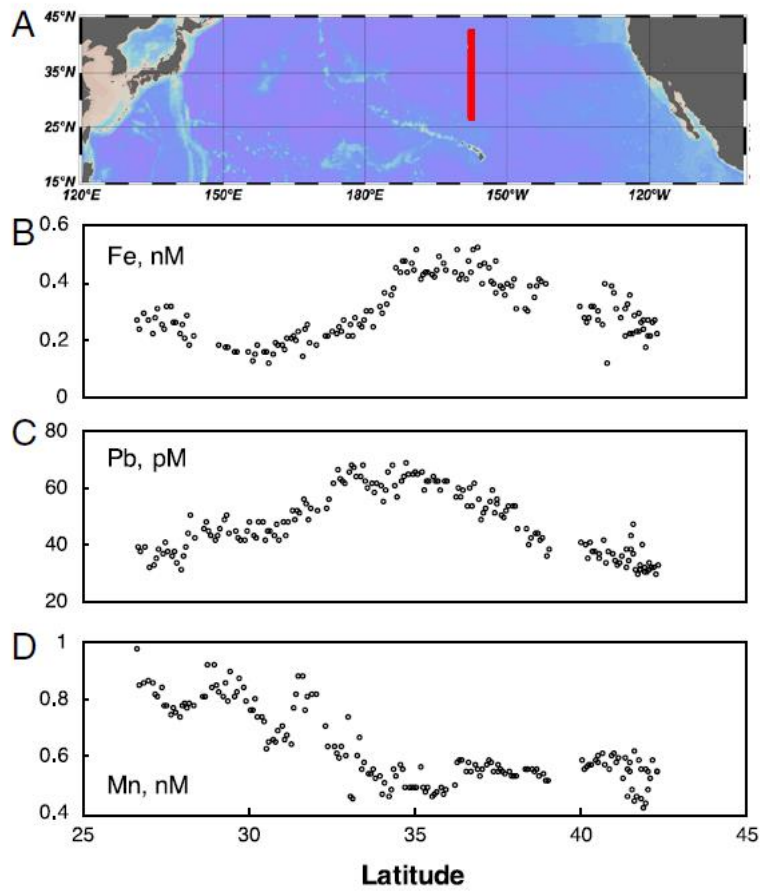
Figure 1. High-resolution distribution of iron (Fe), lead (Pb), and manganese (Mn) across the North Pacific Ocean at 158°W from 21° to 42°N. (A) The red line indicates the cruise track. Samples were collected during the northbound leg. (B) Fe surface concentrations. (C) Pb surface concentrations. (D) Mn surface concentrations.

Figure 2. (A) Distribution of surface Fe concentrations and stable isotope ratios (δ^{56}Fe) along the transect.

(B) Pb isotope composition of seawater from the North Pacific Ocean compared to various Pb sources:

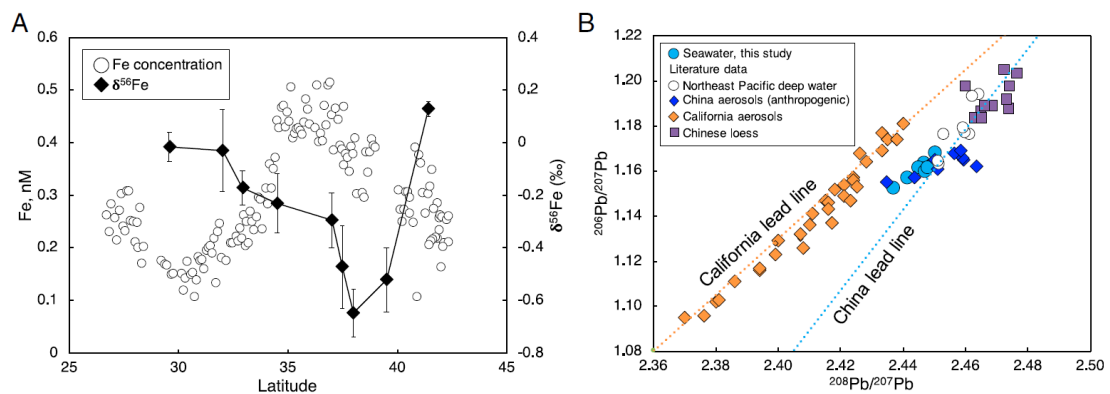North Pacific Ocean deep-water samples collected close to Hawaii below 500 m; Chinese aerosol samples collected since 2014 from sites with high levels of industrial emission; aerosols from California, which probably reflect a mixture between anthropogenic and natural Pb isotopes; Chinese loess samples. Data used to assess the isotopic composition of China and California lead lines are provided in SI Appendix, Table S1. Both Fe and Pb isotopes were measured from the same nine large-volume samples collected during the northbou
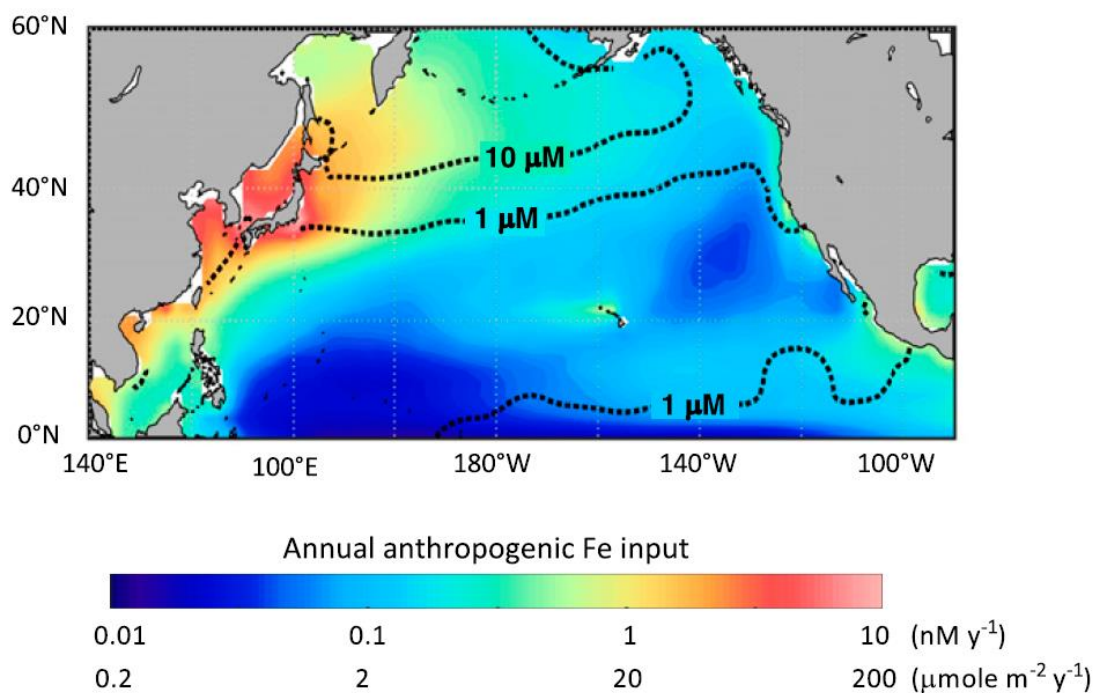
Figure 3. Annual anthropogenic Fe input in the North Pacific Ocean. The likely region of anthropogenic Fe input overlaps with HNLC regions in the North Pacific Ocean. Annual anthropogenic Fe inputs are calculated at our study site, and then extrapolated across the North Pacific Ocean both as a surface flux (μmole m^{-2} y^{-1}) and a concentration flux assuming a 20-m mixed layer and 1-y residence time (nM y^{-1}) using anthropogenic mass deposition fluxes from Brahney et al. and Chien et al. . Contours are World Ocean Atlas annual mean NO$_3$, highlighting HNLC waters in the subarctic North Pacific Ocean.

3. Li 同位素定量揭示硅质岩浆喷发过程中挥发分损失的时间尺度

翻译人：冯婉仪 fengwy@sustech.edu.cn

摘要：大多数爆发性的硅质火山在两次喷发事件之间会沉寂数千年。火山从静止状态转变为喷发状态所需的时间对于解释监测信号和提高生活在活火山附近的人们的安全至关重要。我们利用一种基于黄石火山系统（美国爱达荷州和怀俄明州）的 Mesa Falls 凝灰岩中斜长石晶体的锂同位素（δ^7Li）和元素浓度剖面的新方法解决了这个问题，限定了挥发分的去气作用发生在火山喷发前几十分钟之内。在这短暂的时间里，从斜长石核部到边部，其 Li 含量下降了 4 - 10 倍，并且伴随着 δ^7Li 高达 10‰的增加，这反映了在斜长石核部与去气的贫 Li 熔体之间，由扩散作用驱动的平衡过程。在这项研究中获得的新的时间尺度显示了岩浆挥发分含量在火山喷发过程中快速变化的潜力。

ABSTRACT: Most explosive, silicic volcanoes spend thousands of years in repose between eruptive events. The timing of the switch from repose to eruption is key to interpreting monitoring signals and improving the safety of people living close to active volcanoes. We addressed this question using a novel technique based on lithium isotopic (δ^7Li) and elemental concentration profiles within plagioclase crystals from the Mesa Falls Tuff of the Yellowstone volcanic system (Idaho and Wyoming, USA), constraining volatile degassing to occur on minimum time scales of tens of minutes prior to eruption. During this ephemeral time, Li abundances drop by a factor of four to 10 from crystal cores to rims, accompanied by an increase in δ^7Li of as much as 10‰, reflecting diffusion-driven equilibration between plagioclase cores and outgassed, Li-poor melt. New times scales obtained in this study show the potential for rapid syneruptive changes in the volatile inventory of magmas.
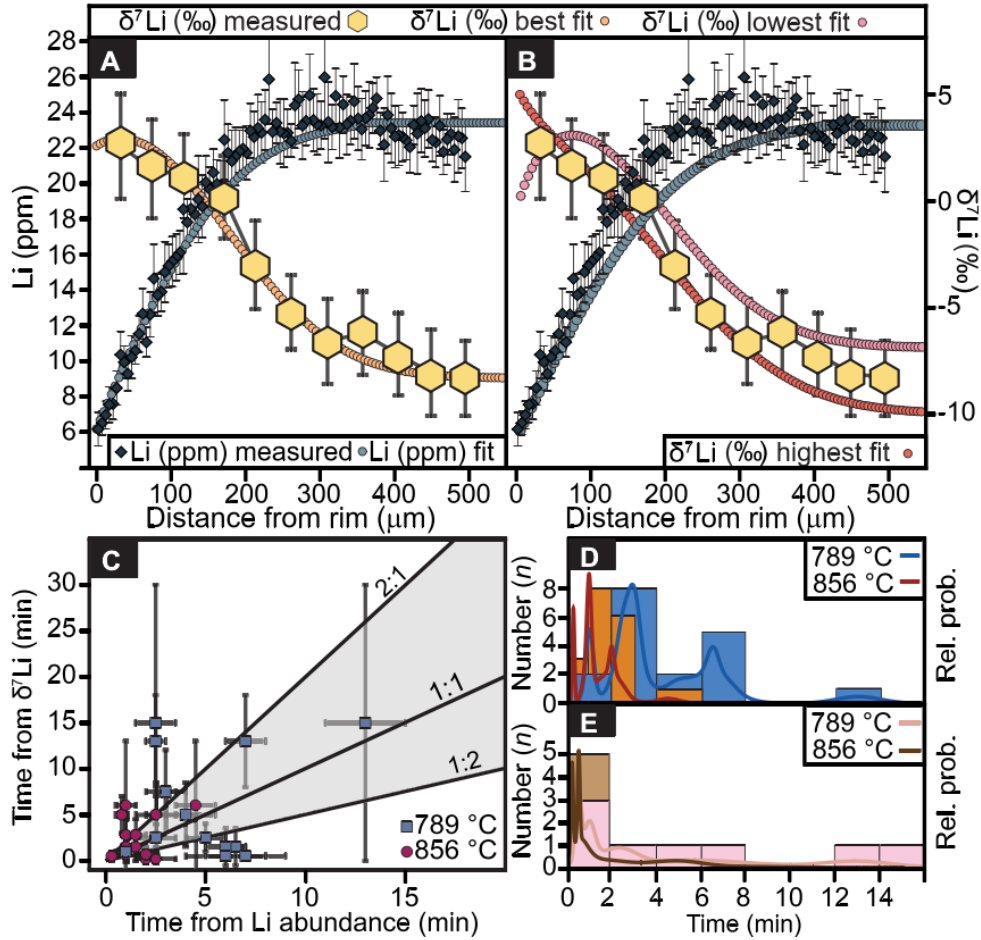
Figure 1. Example of one-dimensional Li diffusion model for Mesa Falls Tuff plagioclase (Yellowstone volcanic system, Idaho and Wyoming, USA). (A) Representative diffusion profile with measured (blue diamonds) concentration profile and its modeled best fit (blue circles), in situ measured δ^7Li data (yellow hexagons), and best fit for δ^7Li profile (orange circles). (B) Profiles shown in A with boundary conditions set to highest (red) and lowest (pink) isotopic value within analytical error. (C) Comparison of time scales obtained by diffusion modeling of Li concentration (Li abundance) and isotope (δ^7Li) profiles. Blue squares represent time scales at 789 °C, and red circles refer to time scales at 856 °C. Errors are provided as dark gray error bars. Lines labeled 1:1, 2:1, and 1:2 and the gray shaded area indicate the field of best agreement between time scales obtained for Li concentration and isotope profiles. (D) Time scales obtained from Li concentration profiles (n = 18) shown as lines at 789 °C (blue) and 856 °C (red) for their relative probability (Rel. prob.). Histogram (789 °C in blue, 856 °C in orange) shows distribution of time scales. (E) Time scales obtained from all eight (two profiles in the same crystal) analyzed δ^7Li profiles at 789 °C (pink) and at 856 °C (brown). Histogram (789 °C in pink, 856 °C in brown) shows distribution of the time scales.

4. CHAOS-7 地磁场模型和观测到的南大西洋异常的变化

翻译人：李园洁 liyj3@sustech.edu.cn

摘要：本文中作者展示了 1999-2020 期间随时间变化的近地球地磁场的 CHAOS-7 模型，该模型是基于近地轨道卫星 Swarm，CryoSat-2，CHAMP，SAC-C 和 Ørsted 的磁场观测值以及地面观测站月均值的年变化。CHAOS-7 模型包括一个随时间变化的球谐函数达 20 阶的内部场，一个加入 25 阶以上 LCS-1 岩石圈磁场模型的稳定内部场，一个磁层场模型和其感应部分，描述卫星矢量磁力仪定位的欧拉角估计值和 CryoSat-2 的磁力仪校正参数。只有暗区域满足严格地磁平静期标准(包括所有纬度的 IMF Bz 和 By 的条件)的数据才用来估计地磁场。模型参数用一个迭代重加权正则化最小二乘程序；相比之前的 CHAOS 模型，随时间变化内部场正则化在高阶球谐函数不加约束。作者用 CHAOS-7 模型来研究自 2014 年南大西洋弱磁场异常的演化和太平洋区域的磁场快速变化。在地球表面南大西洋异常的次小值在非洲西南部非常明显。将核幔边界径向场和地面强度联系起来的格林函数表明，这种特征与南非下面一个逆流特征的运动和演化有关。范围的持续扩大和主要异常的减弱与南美洲之下的逆流向西运动和汇聚有关。在太平洋地区，2015 到 2018 期间地球表面地磁场径向分量的二阶时间导数(加速度)发生正负变化。这个加速度变化主要形式是局部东西向的偶极子。地面上清楚记录到这个变化，比如 Honolulu 台站，Swarm 观测站在太平洋中部和西部更广泛的区域也可看到。向下延拓到核幔边界，发现这个事件起源于 2017 年太平岩中部和西部之下低纬度磁场加速度变化。

ABSTRACT：We present the CHAOS-7 model of the time-dependent near-Earth geomagnetic field between 1999 and 2020 based on magnetic field observations collected by the low-Earth orbit satellites Swarm, CryoSat-2, CHAMP, SAC-C and Ørsted, and on annual differences of monthly means of ground observatory measurements. The CHAOS-7 model consists of a time-dependent internal field up to spherical harmonic degree 20, a static internal field which merges to the LCS-1 lithospheric field model above degree 25, a model of the magnetospheric field and its induced counterpart, estimates of Euler angles describing the alignment of satellite vector magnetometers,

and magnetometer calibration parameters for CryoSat-2. Only data from dark regions satisfying strict geomagnetic quiet-time criteria (including conditions on IMF Bz and By at all latitudes) were used in the field estimation. Model parameters were estimated using an iteratively reweighted regularized least-squares procedure; regularization of the time-dependent internal field was relaxed at high spherical harmonic degree compared with previous versions of the CHAOS model. We use CHAOS-7 to investigate recent changes in the geomagnetic field, studying the evolution of the South Atlantic weak field anomaly and rapid field changes in the Pacific region since 2014. At Earth's surface a secondary minimum of the South Atlantic Anomaly is now evident to the south west of Africa. Green's functions relating the core-mantle boundary radial field to the surface intensity show this feature is connected with the movement and evolution of a reversed flux feature under South Africa. The continuing growth in size and weakening of the main anomaly is linked to the westward motion and gathering of reversed flux under South America. In the Pacific region at Earth's surface between 2015 and 2018 a sign change has occurred in the second time derivative (acceleration) of the radial component of the field. This acceleration change took the form of a localized, east-west oriented, dipole. It was clearly recorded on ground, for example at the magnetic observatory at Honolulu, and was seen in Swarm observations over an extended region in the central and western Pacific. Downward continuing to the core-mantle boundary, we find this event originated in field acceleration changes at low latitudes beneath the central and western Pacific in 2017.
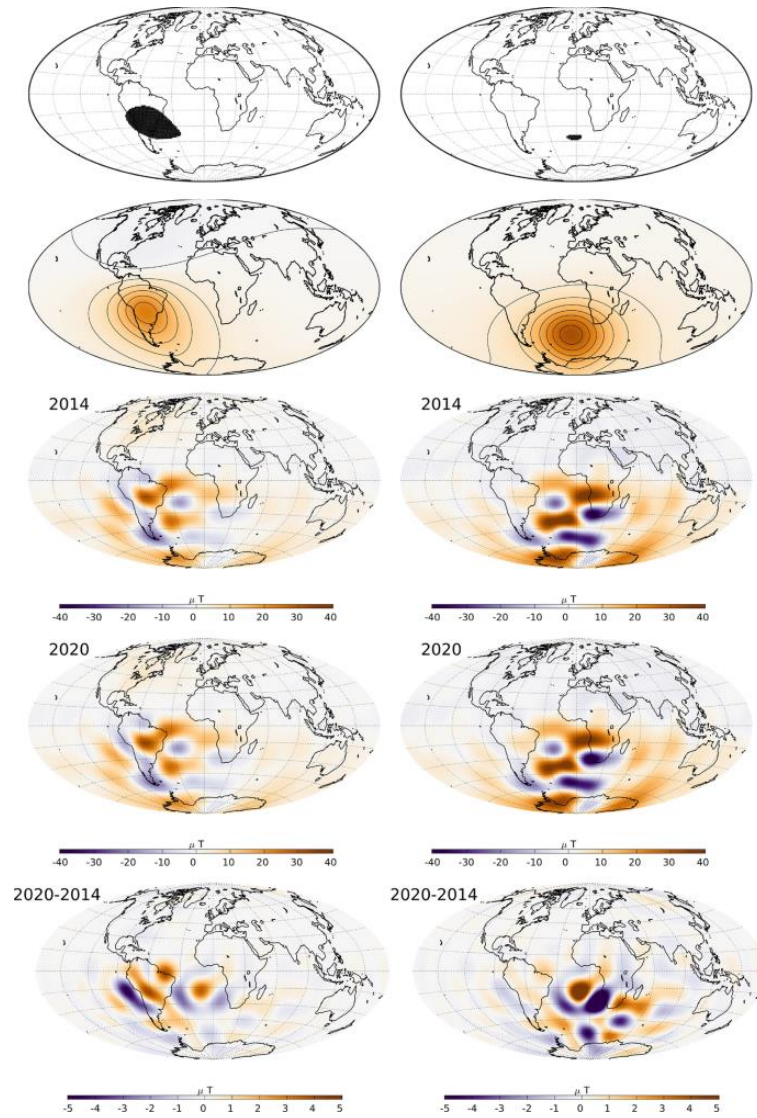
Figure 1. Core-mantle boundary origin of the South Atlantic Anomaly and its recent changes analysed using Green's functions for the Laplace equation under Neumann boundary conditions. Top row: black areas show regions of lowest intensity (under 24,000 nT) selected for analysis, the main anomaly (left column) and the new secondary minimum (right column). 2nd row: combined sensitivities G^{Σ}_{F} (see Eq. (24)) showing the sensitivity of the field intensity, relative to the dipole, to the core–mantle boundary radial field, for each defined region. 3rd row: taking these sensitivities as weights and multiplying by the radial field at the core–mantle boundary. This shows the parts of the radial field at the core-mantle boundary that in combination are responsible for the main South Atlantic anomaly (left) and the new secondary minimum (right), respectively, in 2020. Bottom row: change in the sensitivity-weighted radial field at the core-mantle boundary between 2014 and 2020, showing the origin of field intensity changes for the selected regions at Earth's surface.

5. 巴比伦毁灭期间耶路撒冷的地球磁场：地磁场变化的独特参考和古地磁定年的锚点

翻译人：柳加波

摘要：考古材料的古地磁研究对于了解过去的地磁场行为至关重要。由于通常很难准确地确定考古材料中古地磁磁记录的准确年代，因此在古地磁数据库中通常存在较大的年龄不确定性和差异，从而限制了将这些数据用于古地磁场建模和古地磁定年的能力。本文，我们重建了具有精确年代的，在公元前 596 年秋天，耶路撒冷的古地磁场方向和强度数据。这个时间即巴比伦军队对这座城市进行大火摧毁的日期，也标志着黎凡特铁器时代的终结。我们分析了 54 个地板残片，这些地板具有空前的建筑质量，是在一座大型纪念性建筑物中发掘的，该建筑物曾经是精英或公共建筑，并在大火中倒塌。从重建的古磁方向，我们认为，倾斜的地板残片最初是建筑物第二层地板的一部分，并且在倒塌后被冷却。这将地磁记录的时间与销毁日期牢固地联系在一起。相对较高的地磁场强度，即虚拟轴向偶极矩（VADM）高达 148.9 ±3.9 ZAm^2，并伴随着地心轴向偶极子场（GAD）的倾角和 8.3° 正偏角。这表明公元前 6 世纪的地磁场是不稳定的，并且重新定义了黎凡特铁器时代磁异常的持续时间。具有精准年代的古地磁重建，使我们能够约束其他铁器时代发现的年代，并解决有关皇家朱迪安盖章瓶柄（royal Judean stamped jar handles）的作用和年代的长期考古和历史争论。本研究证明了从历史性毁灭中获得的古地磁数据如何作为古地磁测年的锚点，以及在放射性碳不足以用于高分辨率测年的时期内其特殊的效力。

ABSTRACT: Paleomagnetic analysis of archaeological materials is crucial for understanding the behavior of the geomagnetic field in the past. As it is often difficult to accurately date the acquisition of magnetic information recorded in archaeological materials, large age uncertainties and discrepancies are common in archaeomagnetic datasets, limiting the ability to use these data for geomagnetic modeling and archaeomagnetic dating. Here we present an accurately dated

reconstruction of the intensity and direction of the field in Jerusalem in August, 586 BCE, the date of the city's destruction by fire by the Babylonian army, which marks the end of the Iron Age in the Levant. We analyzed 54 floor segments, of unprecedented construction quality, unearthed within a large monumental structure that had served as an elite or public building and collapsed during the conflagration. From the reconstructed paleomagnetic directions, we conclude that the tilted floor segments had originally been part of the floor of the second story of the building and cooled after they had collapsed. This firmly connects the time of the magnetic acquisition to the date of the destruction. The relatively high field intensity, corresponding to virtual axial dipole moment (VADM) of 148.9 ± 3.9 ZAm2, accompanied by a geocentric axial dipole (GAD) inclination and a positive declination of 8.3°, suggests instability of the field during the 6th century BCE and redefines the duration of the Levantine Iron Age Anomaly. The narrow dating of the geomagnetic reconstruction enabled us to constrain the age of other Iron Age finds and resolve a long archaeological and historical discussion regarding the role and dating of royal Judean stamped jar handles. This demonstrates how archaeomagnetic data derived from historically-dated destructions can serve as an anchor for archaeomagnetic dating and its particular potency for periods in which radiocarbon is not adequate for high resolution dating.
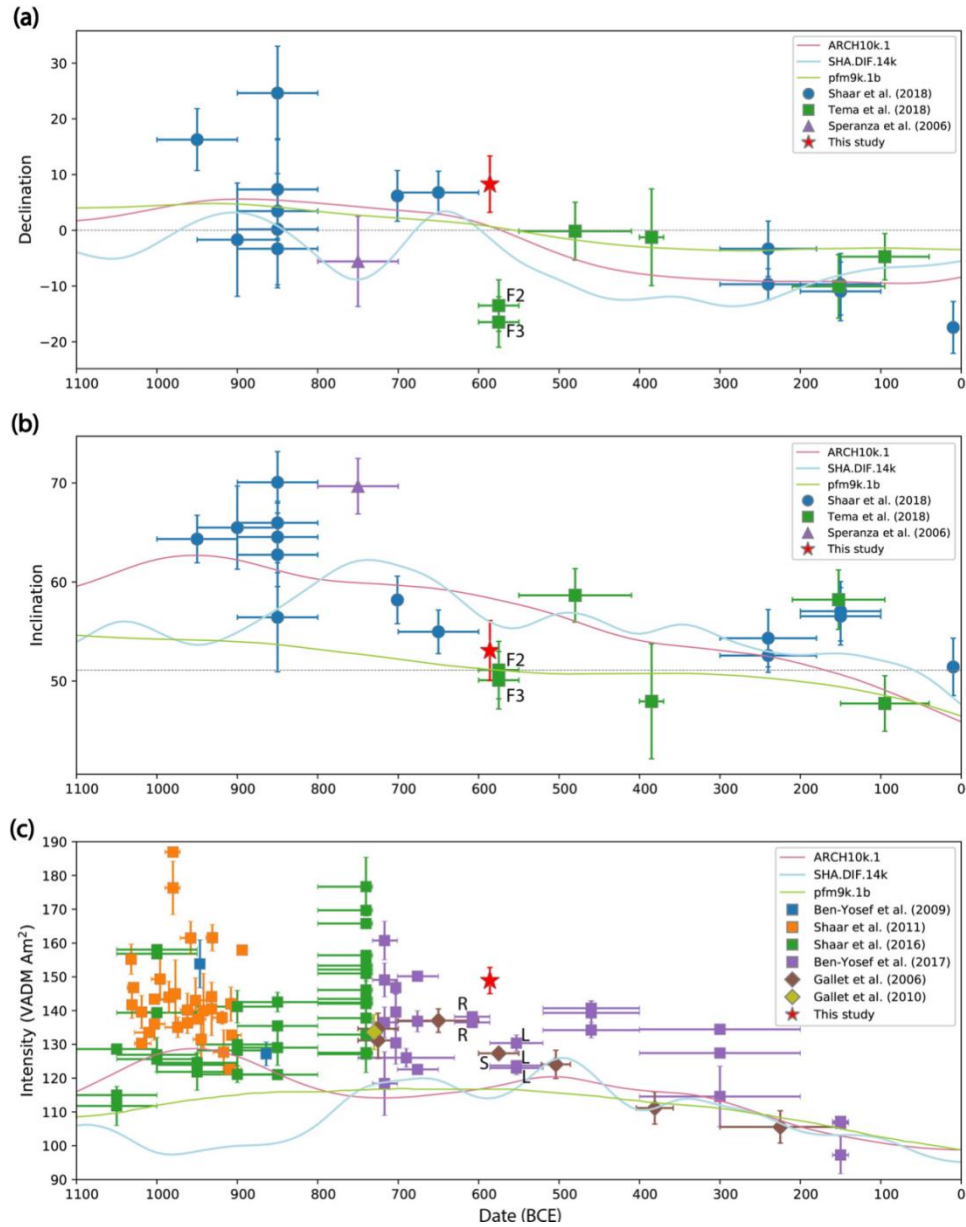
Figure 1. Archaeomagnetic direction and intensity data in the Levant (Israel, Syria, Jordan, Cyprus). The average results from the 586 BCE destruction layer in Jerusalem are represented by red stars and error bars (a) Declination. (b) Inclination. All directions are relocated to Jerusalem. The dashed grey lines represent the direction of a geocentric axial dipole (GAD) field in Jerusalem. The results of two chambers of a twin furnace from the Agia Varvara-Almyras archaeological site are marked "F2" and "F3". (c) Paleointensity given as the corresponding virtual axial dipole moment (VADM). The colored curves represent three different global geomagnetic models [1–3]. The results of two types of Judean stamped jar handles are marked: Rosette jar handles with the letter "R" and Lion jar handles with the letter "L". The result from Sheikh Hamad site is marked with the letter "S" (see text for details).

6. 通过重力和磁异常模拟西西里岛的地壳结构

翻译人：曹伟 11930854@QQ.com

摘要：本研究的目的是模拟西西里岛（意大利）的主要地壳和热界面，这是了解非洲板块和欧洲板块碰撞边界地质复杂性的关键区域。为此，我们综合测井、地质、热流和地震资料，分析该区的重力场和磁场。为了最准确地描述该地区的地壳结构，我们用不同的方法模拟了碳酸盐和结晶顶面，以及莫霍面和居里等温面。碳酸盐岩台地的重建是在现有地震和钻孔资料约束下，采用非线性三维方法实现的；而晶体顶部、居里点和莫霍面都是通过重磁数据的频谱分析来估算的。结果表明，在西西里岛中部有一个复杂的碳酸盐基底和一个深结晶地壳，Hyblean 高原下有一个显著的隆起。莫霍面和居里等温线表面的分布定义了西西里岛多变的热环境和结构背景，南部和东部地区地壳非常薄，在那里发现了高热流，而 caltanissetta 盆地下方则是深冷的地壳。

ABSTRACT: We aim at modeling the main crustal and thermal interfaces of Sicily (Italy), a key area for understanding the geological complexity at the collisional boundary between the African and European plates. To this end, we analyze the gravity and magnetic fields, integrated with information from well logs, geology, heat flow, and seismic data. In order to make the most accurate description of the crustal structure of the area, we modeled with different methodologies the carbonate and crystalline top surfaces, as well as the Moho and the curie isotherm surface. The reconstruction of the carbonate platform is achieved using a nonlinear 3D method constrained by the available seismic and borehole data. The crystalline top, the curie, and the Moho are instead estimated by spectral analysis of both gravity and magnetic data. The results show a complex carbonate basement and a deep crystalline crust in central Sicily, with a prominent uplift beneath the Hyblean plateau. Maps of the Moho and the Curie isotherm surface define a variable thermal and structural setting of Sicily, with very thin crust in the southern and eastern sectors, where high heat flow is found, and deep and cold crust below the caltanissetta Basin.
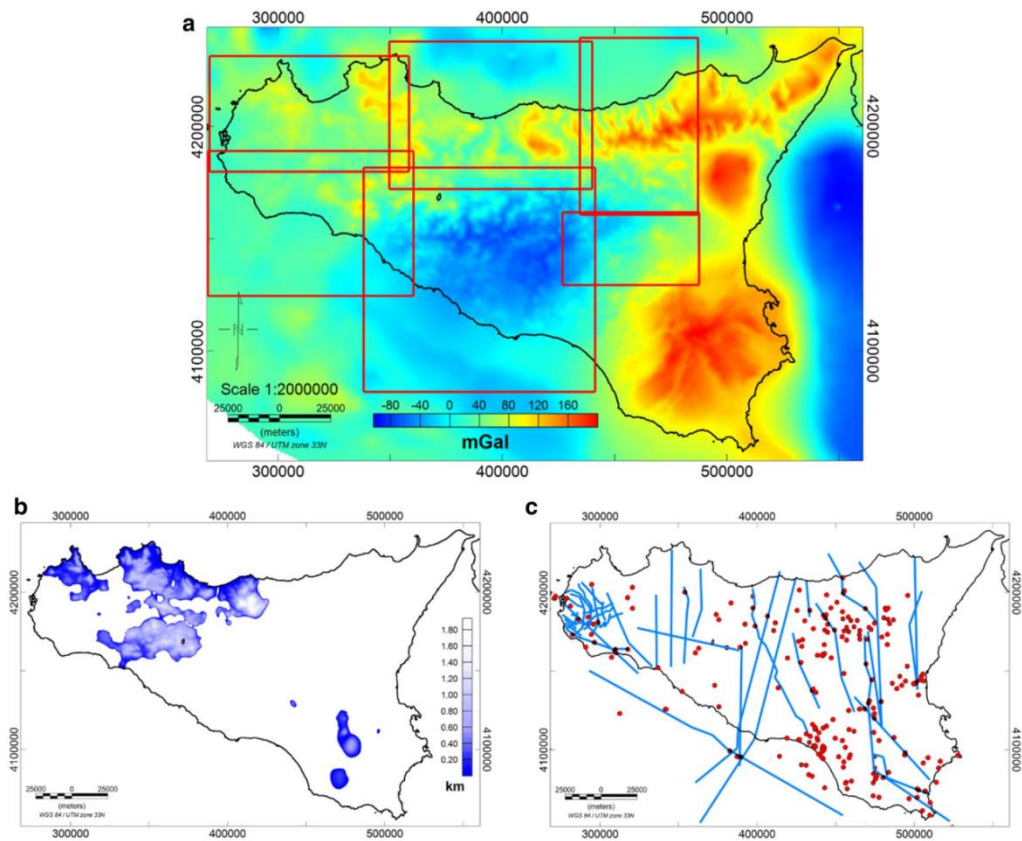
Figure 1. (a) Free-air gravity field map with the subareas selected to compute the carbonate basement (red rectangles); (b) Geological data of the outcropping Mesozoic carbonates; (c) well logs (red dots) and seismic profiles (blue lines) used to constrain the carbonate basement model.

7. 来自亚北极、北太平洋和格陵兰的风尘通量记录:对大气向格陵兰输送
的影响以及风尘作为年代地层工具的应用

翻译人：王敦繁 dunfan-w@foxmail.com

摘要：我们通过底特律海山的岩心展示了过去 27000 年以来西亚北极北太平洋(SNP)风尘通量的最新记录。将 SNP 风尘记录与北格林兰冰芯(NGRIP)的记录进行对比，可以发现，在最后一次冰川消冰期，两个地区的风尘变化幅度有显著差异，而突变的时间是同步的。如果 SNP 中的风尘沉降真实地记录了其在东亚源区的活动，那么其相对变化的差异一定反映了大气风尘向格陵兰岛输送时的气候变化。基于同时期的 SNP 风尘和格陵兰岛的变化,我们把冰消期通量记录的突然转换对应到相应的过渡的年代，确定 NGRIP 粉尘通量记录提供了一个新的海洋沉积物的年代地层技术从亚北极太平洋。这项技术的结果得到了放射性碳定年法的补充，它使我们能够独立地限制放射性碳古时代。我们发现古地磁年龄在 11653 年前为 745±140 年，在 14630 年前为 680±228 年，在 23290 年前为 790±498 年。我们重建的古地磁年龄与 SNP 西部的现代地面水水库年龄一致。来自亚南极大西洋和赤道太平洋的风成尘埃记录与来自南极的冰芯记录之间有良好的时间同步性，支持了所提出的风尘方法在全球其他海洋区域更广泛应用的可靠性。

ABSTRACT: We present a new record of eolian dust flux to the western Subarctic North Pacific (SNP) covering the past 27,000 years based on a core from the Detroit Seamount. Comparing the SNP dust record to the North Greenland Ice Core Project (NGRIP) ice core record shows significant differences in the amplitude of dust changes to the two regions during the last deglaciation, while the timing of abrupt changes is synchronous. If dust deposition in the SNP faithfully records its mobilization in East Asian source regions, then the difference in the relative amplitude must reflect climate-related changes in atmospheric dust transport to Greenland. Based on the synchronicity in the timing of dust changes in the SNP and Greenland, we tie abrupt deglacial transitions in the 230Th-normalized 4He flux record to corresponding transitions in the well-dated NGRIP dust flux

record to provide a new chronostratigraphic technique for marine sediments from the SNP. Results from this technique are complemented by radiocarbon dating, which allows us to independently constrain radiocarbon paleoreservoir ages. We find paleoreservoir ages of 745 ± 140 years at 11,653year B.P., 680 ± 228 years at 14,630year B.P., and 790 ± 498 years at 23,290year B.P. Our reconstructed paleoreservoir ages are consistent with modern surface water reservoir ages in the western SNP. Good temporal synchronicity between eolian dust records from the Subantarctic Atlantic and equatorial Pacific and the ice core record from Antarctica supports the reliability of the proposed dust tuning method to be used more widely in other global ocean regions.
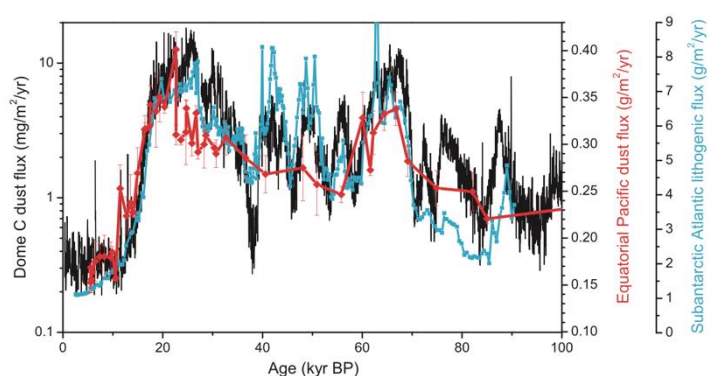

Figure 1. Examples illustrating the potential for global eolian dust records to be used as a chronostratigraphic tool for marine sediment cores. Two marine sediment records of dust flux based on 232Th, one from the equatorial Pacific (red line and diamond symbols; TN013-PC72) [Winckler et al., 2008] and the other from the Subantarctic Atlantic (blue line and square symbols; PS2498-1) [Anderson et al., 2014], showing good temporal synchronicity with the dust flux record from EPICA Dome C in Antarctica (black line) [Lambert et al., 2012] over the last ~100 kyr. Note that the EPICA Dome C ice core record is plotted with a logarithmic scaling.

8. 晚全新世死海沉积物的磁特性对区域水文气候的监测作用

翻译人：李海 12031330@mail.sustech.edu.cn

摘要： 缺氧沉积环境中的成岩作用主要通过碎屑磁铁矿的溶解和自生胶黄铁矿来影响沉积磁性。近期的研究成果指示晚全新世死海沉积物为研究灰砾岩的形成和保存过程及其与不同水文环境的关系提供了机会。磁学数据和孔隙流体参数取自死海西岸 N-S 横断面的三个全新世剖面:Og、Ein-Feshkha 和 Ein-Gedi。北部地区更接近死海的主要淡水来源——约旦河。所有剖面均有钛磁铁矿碎屑，但 Og 和 Ein-Feshkha 的主要磁性特征表现为胶黄铁矿。不同区域之间和区域内的大块岩石磁性数据差异超过 3 个数量级，数值越高表示胶黄铁矿浓度越高。在这三个地点，孔隙流体的盐度与现代和全新世死海盐水相近或更低，其中含有可变和溶解的铁(Fe^{2+})和硫酸盐(SO_4^{2-})。磁性特征的变化反映在铁或硫酸盐微生物减少，控制沉积胶黄铁矿的形成。我们认为，N-S 胶黄铁矿的减少表明，缺氧微生物活动是由不稳定的有机质或活性铁控制的，这些活性铁是由来自约旦河的淡水流入或形成的。因此，胶黄铁矿浓度的变化取决于过去对高盐湖的淡水输入和对淡水来源的接近程度。水文条件和磁性之间的明显关系为追踪死海过去的水文变化提供了一种新的方法。

Abstract: Diagenetic processes in anoxic sedimentary environments influence sediment magnetic properties mainly through dissolution of detrital magnetite and precipitation of authigenic greigite. Recently exposed late Holocene Dead Sea sediments provide an opportunity to study the processes governing greigite formation and preservation, and their relation to different hydrological settings. Magnetic data and pore-fluid compositions were obtained from three Holocene sections along a N-S transect on the western Dead Sea shore: Og, Ein-Feshkha, and Ein-Gedi. The northern sections are closer to the major freshwater source to the Dead Sea – the Jordan River. Detrital titanomagnetite is present at all sections, but greigite is the dominant magnetic phase at Og and Ein-Feshkha. Bulk rock magnetic data varies between and within the sections by over three orders of magnitude, where higher values indicate higher greigite concentrations. At the three sites, pore-fluids have similar or lower salinity than the modern and Holocene Dead Sea brine, with variable and dissolved iron (Fe^{2+})

and sulfate (SO_4^{2-}). Magnetic property changes are reflected by iron and/or sulfate microbial reduction that controlled sedimentary greigite formation. We propose that the N-S greigite decrease suggests that anoxic microbial activity was controlled by labile organic matter and/or reactive iron brought by, or formed as a result of, freshwater influx from the Jordan River. Hence, greigite concentration changes depended on past freshwater input to the hypersaline lake and proximity to the freshwater source. The apparent relationship between hydrological conditions and magnetic properties provides a new method to trace past hydrological changes in the Dead Sea.
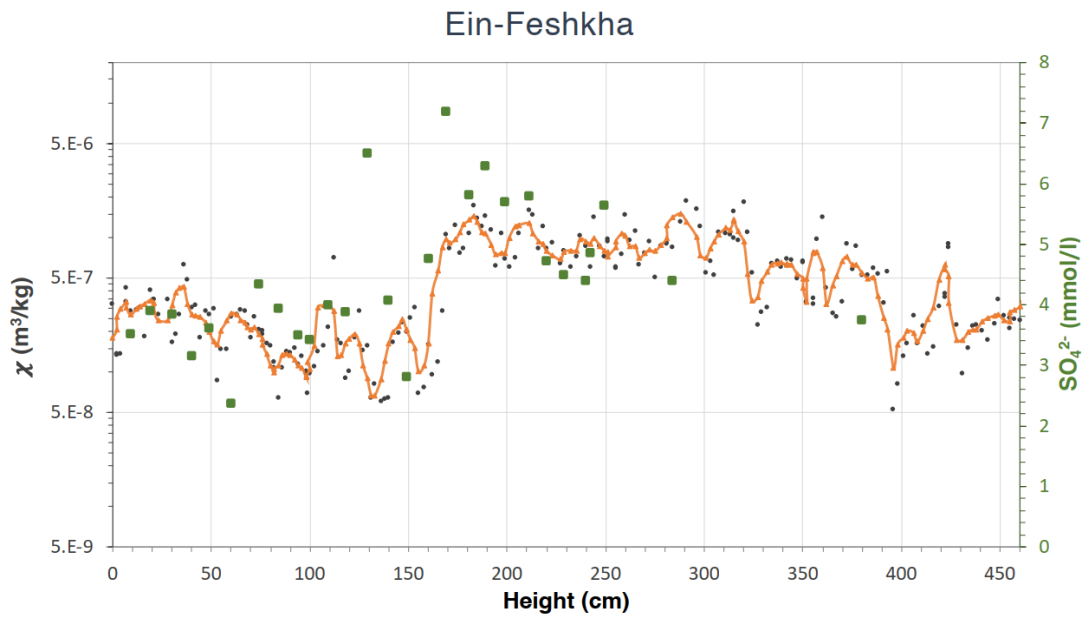

Figure 1. Depth profiles of susceptibility (χ) and sulfate concentration in pore-fluids at EF. χ changes correlate with sulfate concentration changes. The orange line is a 4-point running average through the χ profile for the Ein-Feshkha section

9. 南极洲罗斯海西部区域冰盖中全新世的突然减薄

翻译人：张亚南 zhangyn3@mail.sustech.edu.cn

摘要：注出冰川（outlet glaciers）排出南极冰盖的大部分冰流（ice flow）。理论和数值模型表明，当地的基底地貌在调节冰川出口对气候变暖的响应中发挥着关键作用，可能导致冰川后撤的延迟、异步或增强。然而，现代观测时间较短，无法评估当地或区域控制是否在时间尺度上主导了冰盖的反应，而这对于理解本世纪及未来冰盖质量损失至关重要。最近的地质历史记录是我们能够了解这种百年尺度的冰原变化。我们展示了毗邻罗斯海的莫森冰川的宇宙成因地表暴露年代学，该区域经历了末次冰盛期以来动态的冰盖（marine-based ice sheet）后撤。我们的数据显示在 7.5-4.5ka 之间冰盖突然减薄了至少 220m，随后逐渐减薄直到最近一千年。莫森冰川变薄的时间、速度和幅度与向南 100km 处的麦凯冰川（Mackay Glacier）十分相似，两处冰川的记录都表明全新世中期大范围冰川的突然消融。尽管罗斯海西部地形复杂，这种情况还是发生了，这意味着一个控制冰盖后撤的外部驱动力。通过对比区域海平面和温度的变化，表明海洋水体变暖极有可能导致冰盖后撤和冰量的减少，然后由于冰盖的不稳定性而加速这一过程。

ABSTRACT: Outlet glaciers drain the majority of ice flow in the Antarctic ice sheet. Theory and numerical models indicate that local bed topography can play a key role in modulating outlet glacier response to climate warming, potentially resulting in delayed, asynchronous, or enhanced retreat. However, the period of modern observations is too short to assess whether local or regional controls dominate ice sheet response on time scales that are critical for understanding ice sheet mass loss over this century and beyond. The recent geological past allows for insight into such centennial-scale ice sheet behavior. We present a cosmogenic surface-exposure chronology from Mawson Glacier, adjacent to a region of the Ross Sea that underwent dynamic marine-based ice sheet retreat following the Last Glacial Maximum. Our data record at least 220 m of abrupt ice thinning between 7.5 and 4.5 ka, followed by more gradual thinning until the last millennium. The timing, rates, and magnitudes of thinning at Mawson Glacier are remarkably similar to that documented 100 km to

the south at Mackay Glacier. Together, both outlet glaciers demonstrate that abrupt deglaciation occurred across a broad region in the Mid-Holocene. This happened despite the complex bed topography of the western Ross Sea and implies an overarching external driver of retreat. When compared to regional sea-level and ocean-temperature changes, our data indicate that ocean warming most likely drove grounding-line retreat and ice drawdown, which then accelerated as a result of marine ice sheet instability.
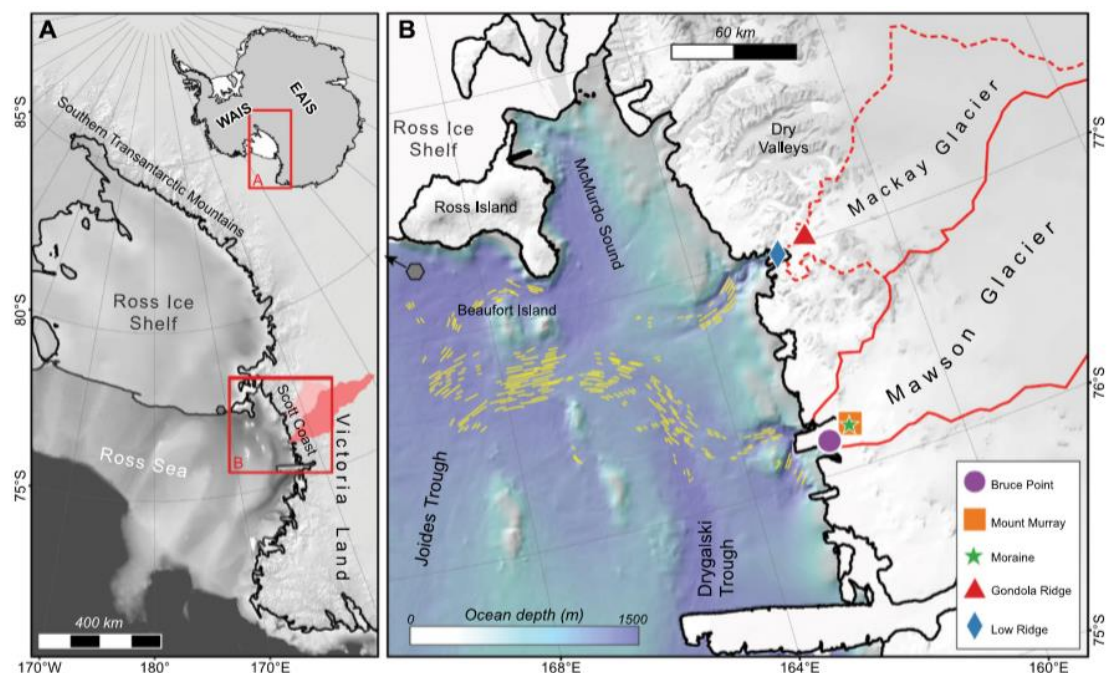

Figure 1. Study region. **(A)** Ross Sea sector of Antarctica, which drains both West Antarctic (WAIS) and East Antarctic (EAIS) ice sheets. **(B)** Map of the Scott Coast region in the western Ross Sea. Records of past ice thickness change come from Mawson Glacier (Bruce Point and Mount Murray) and Mackay Glacier (Low Ridge and Gondola Ridge). Megascale glacial lineations mapped on the seafloor are shown as yellow lines, and gray hexagon denotes the location of sediment core CH-2 (McKay et al., 2016).
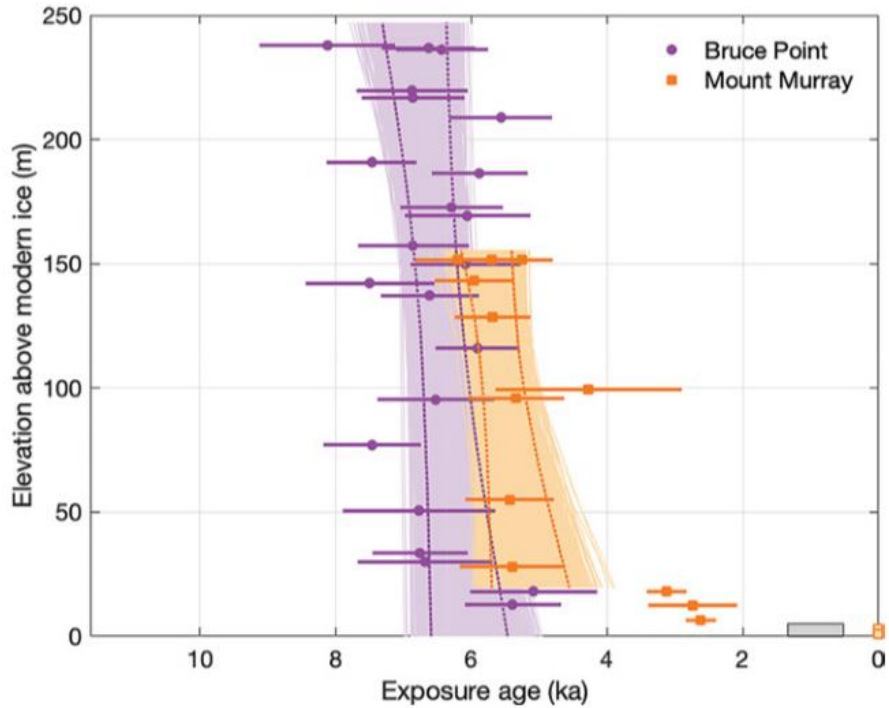
Figure 2. Holocene exposure ages from Mawson Glacier (Antarctica) plotted as a function of elevation. Samples identified as potential outliers are not included here, but the full data set is plotted in Figure S3 (see footnote 1). Two "modern" samples at Mount Murray are included as pale squares (0 ka). Ages are shown as the mean with 1σ uncertainty. Modeled random linear regressions of the abrupt thinning episode are shown for each transect (dotted lines denote 95% confidence bounds). The age uncertainty range (1.3-0.5 ka) for the Mount Murray moraine is plotted as a horizontal gray bar.
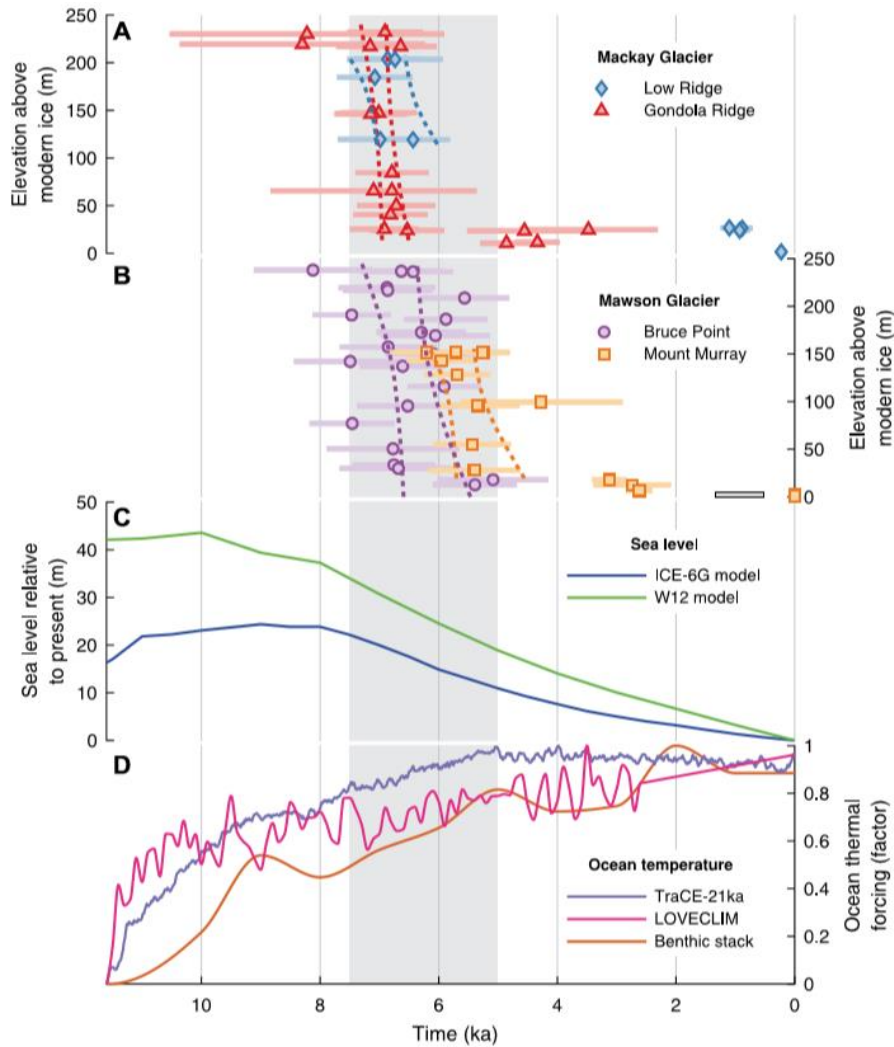
Figure 3. Deglaciation records of the western Ross Sea (Antarctica) and potential forcings. **(A)** Exposure ages versus relative elevation at Mackay Glacier (Jones et al., 2015), with dotted lines denoting 95% confidence bounds from linear regression analysis. Ages are shown as the mean with 1σ uncertainty. **(B)** Exposure ages at Mawson Glacier, as shown in Figure 2. **(C)** Local sea-level change in the western Ross Sea from ICE-6G (Argus et al., 2014) and W12 (Whitehouse et al., 2012) glacial isostatic adjustment models. **(D)** Model- and proxy-based ocean thermal forcings, similar to those used by Lowry et al. (2019). Temperature anomalies from the TraCE-21ka data set (http://www.cgd.ucar.edu/ccr/TraCE/) and LOVECLIM model (https://www.elic.ucl.ac.be/modx/index.php?id=81) (Ross Sea, 400 m depth) (Liu et al., 2009; Menviel et al., 2011) and the global benthic $\delta^{18}O$ stack (Lisiecki and Raymo, 2005) have been scaled to 0 to 1 for the Holocene. Gray band in each plot highlights the period of abrupt outlet glacier thinning (7.5–5 ka).

10. 磁组构研究的当前挑战与未来发展

翻译人：张伟杰 12031188@mail.sustech.edu.cn

摘要：磁组构作为矿物组构的代替指标以及用来校正古地磁数据被广泛地应用，也被提出用于量化孔隙组构。今天对于磁各向异性的理解与解释得益于几十年对矿物与岩石属性各向异性的精细观测，建立和检验了磁组构与矿物组构之间的经验关系，发展了定量各向异性的模型。每次进展之前都有一些令人困惑的观察结果，也就是说，根据当时现有的模型无法解释数据，例如，"斜"或"逆"组构，或依赖于岩性的各向异性-应变关系。这些观察促进了许多实验和数值技术被设计用于识别磁组构和确定它们的起源。尽管磁组构在许多构造问题上得到了成功的应用，但仍有一些现象和测量无法用今天的磁组构理论来解释。为了促进未来的发展，本文将讨论磁组构研究中面临的三个挑战：(1)磁各向异性的实验表征，包括所述张量的非唯一性和非线性；(2)建立各向异性模型，确定磁组构的载体矿物和起源；(3)选择合适的各向异性张量来校正古地磁数据。这里提出的有关挑战将有望帮助确定未来的研究方向，并推进我们的研究。

ABSTRACT: Magnetic fabrics are used extensively as proxies for mineral fabrics and to correct paleomagnetic data, and have been proposed to quantify pore fabrics. Today's understanding and interpretation of magnetic anisotropy benefits from decades of carefully observing anisotropic mineral and rock properties, establishing and testing empirical relationships between magnetic and mineral fabrics, and developing models to quantify aspects of anisotropy. Each advance was preceded by some puzzling observations, i.e., data that could not be explained based on the models available at the time, e.g., 'oblique' or 'inverse' fabrics, or lithology-dependent anisotropy-strain relationships. These observations led to numerous experimental and numerical techniques designed to characterize magnetic fabrics and determine their origin. Despite the successful application of magnetic fabrics in many structural and tectonic problems, there are still phenomena and measurements that cannot be explained based on today's magnetic fabric theory. With the purpose of fostering future development, I will touch on three main areas where I see challenges in magnetic

fabric research: (1) Experimental characterization of magnetic anisotropy, including the non-uniqueness of reported tensors, and non-linearity; (2) anisotropy modelling and defining the carrier minerals and origin of the magnetic fabric; (3) selection of adequate (sets of) anisotropy tensors to correct paleomagnetic data. The description of the challenges presented here will hopefully help define directions for future research, inform those that are new to anisotropy, and advance our field.
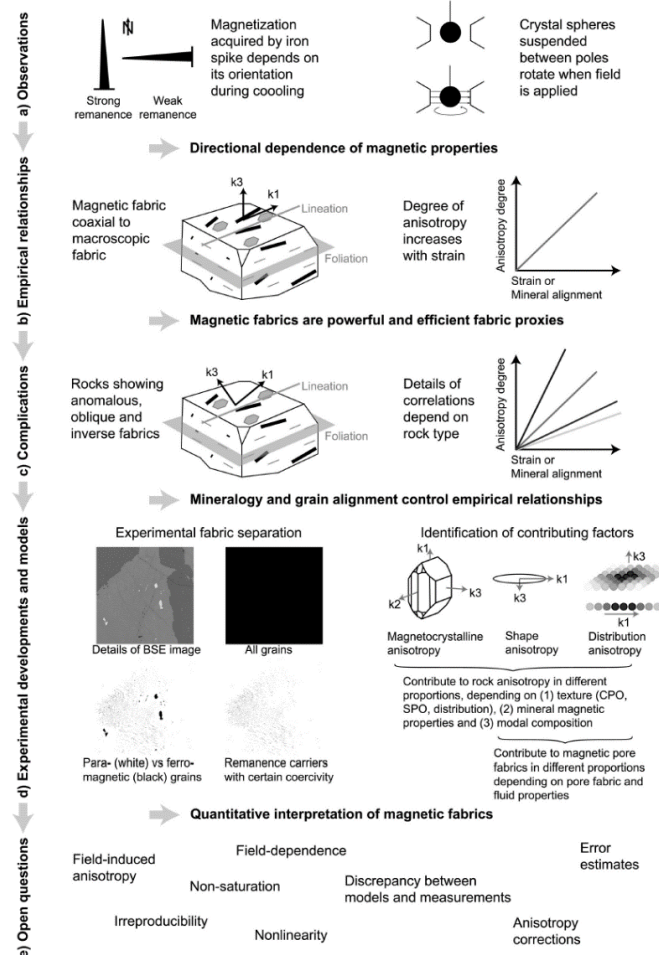

Figure 1. Very brief history of the evolution of our understanding on magnetic fabrics (a-d). New insights and theories were followed by 'complications', i.e., observations that could not be explained by existing theories. Seeking an explanation for these 'abnormal' behaviours eventually led to the development of new theories and an increased understanding about the sources of magnetic anisotropy. (e) The open questions (or complications) discussed in this paper show some of the gaps in our current understanding of magnetic fabrics, and will again lead to new and better theories in the future.

11. 安达曼海沉积物粒度的端元模型指示全新世印度夏季风变化

翻译人：杨会会 11849590@mail.sustech.edu.cn

摘要：一直以来，印度夏季风（ISM）在全新世早期还是中期达到最强是一个较有争议的问题。本研究对安达曼海的一根长 157cm，覆盖过去 11.2 kyr 的钻孔岩芯柱 ADM-C1 进行了粒度测量。采用对数正态参数的端元模型，分离出四个端元。对不同粒度端元的来源分析表明，EM1 和 EM2 可能分别与上层悬浮物和底栖浑浊层的迁移有关。而 EM3 和 EM4 则分别与季风沉积和极端事件下的沉积密切相关。EM3 受控于印度夏季风强度，并由印度夏季风输送到海中，EM3 比例的增加反映了印度夏季风强度增强，反之亦然。EM3 的变化被用来解释 ISM 变化的 3 个阶段：（1） 11.2–9.1kyr，EM3 相对较低，指示 ISM 相对较弱；（2）9.1-4.5 kyr，EM3 大幅度增加，指示 ISM 增强；（3）4.5-0 kyr，EM3 逐渐下降，指示 ISM 逐渐减弱。全新世 ISM 最大期开始于 9.1kyr，而不是在全新世早期，这可能部分是由于全新世早期大西洋经向翻转环流(AMOC)较弱，导致陆地和印度洋之间的陆海热对比减弱；另外一个原因可能是残存的北半球冰盖阻碍了热带辐合带（ITCZ）的北移。7 次相对短暂的 ISM 强度下降(事件 7、7、5、4、3、2、1)分别发生在约 10.3、9.7、7.3、5.7、4.2、2.4 和 0.8 kyr BP。在年龄经度范围内，它们与北大西洋沉积中冰筏碎屑的增加对应，表明在千年尺度上 ISM 强度的变化主要受北半球高纬度地区气候过程的影响。

Abstract: Whether the Indian Summer Monsoon (ISM) Maximum started in the early Holocene or middle Holocene remains a controversial issue. Grain-size measurements were conducted on 157-cm-long core ADM-C1 from the Andaman Sea; the core spanned the last 11.2 kyr BP. Four end-members (EMs) were unmixed using lognormal parametric end-member modeling. Genetic analyses of the grain-size EMs suggested the EM1 and EM2 may correlate with suspension in the upper layers and transportation in the benthic nepheloid layer, respectively, while the EM3 and EM4 were tied with deposition affected by monsoonal currents and sedimentation under extreme events, respectively. The EM3 was dominated by ISM intensity and transported by summer monsoon

currents, with increase in the proportion of EM3 reflecting increasing ISM intensity, and vice versa. Variations in EM3 were used to defne three stages of ISM evolution, as follows: (1) During 11.2-9.1 kyr BP, EM3 was relatively low, indicating a weak ISM; (2) during 9.1–4.5 kyr BP, EM3 increased substantially, indicating a strengthened ISM; (3) during 4.5-0 kyr BP, EM3 decreased gradually, suggesting a gradual weakening of the ISM. The Holocene ISM Maximum started at ~9.1 kyr BP rather than in the early Holocene, which may have been partly due to the slowdown of the Atlantic meridional overturning circulation (AMOC) during the early Holocene that resulted in a decreased land-sea thermal contrast between the landmass and the Indian Ocean. An additional cause may have been the remnant Northern Hemisphere ice sheets that impeded the northward shift of the Intertropical Convergence Zone (ITCZ). Seven relatively brief decreases in the ISM intensity (events 7, 6, 5, 4, 3, 2, 1) occurred at ca. 10.3, 9.7, 7.3, 5.7, 4.2, 2.4, and 0.8 kyr BP, respectively. They corresponded, within the age uncertainties, to the increased supplies of ice-rafted detritus to North Atlantic sediments, implying that changes in the ISM intensity on millennial scale were dominated by climatic processes in northern high latitudes.

12. 碎屑锶同位素地层学研究盆内沉积物循环

翻译人：刘伟 inewway@163.com

摘要：由于沉积物在从源到汇的过程中存在地球化学或地质年代学信号的混合，可能会阻碍地层学中气候和构造信号的重建。约束盆地内沉积物再旋回的时间一直具有挑战性，因为广泛应用的碎屑地质热年代学手段不能记录浅埋藏地质信息。本文应用锶同位素地层学技术对智利岩浆盆地上白垩统 Tres Pasos 组斜坡沉积的再旋回海相贝壳物质进行了研究。94 个样品的 $^{87}Sr/^{86}Sr$ 碎屑年龄表明，大部分(85%)贝壳的年龄比独立约束的沉积年龄大 1-12 Ma。我们认为了贝壳 $^{87}Sr/^{86}Sr$ 年龄与地层沉积年龄之差，代表了沉积物在百万年的时间尺度内的再旋回的时间。我们还利用贝壳标本类型来推断盆内物源的相对位置，其中牡蛎代表浅水源(即近源)，叠瓦蛤代表深水源(即远源)。碎屑锶同位素年代学和贝壳标本类型确定物源这两种手段的结合，有利于确定古代源-汇系统中的沉积物储存和再旋回的时间。

ABSTRACT: Temporary storage of sediment between source and sink can hinder reconstruction of climate and/or tectonic signals from stratigraphy by mixing of sediment tracers with diagnostic geochemical or geochronological signatures. Constraining the occurrence and timing of intrabasinal sediment recycling has been challenging because widely used detrital geo-thermochronology applications do not record shallow burial and subsequent reworking. Here, we apply strontium isotope stratigraphy techniques to recycled marine shell material in slope deposits of the Upper Cretaceous Tres Pasos Formation, Magallanes Basin, Chile. Detrital 87Sr/86Sr ages from 94 samples show that the majority (>85%) of the shells are >1–12 m.y. older than independently constrained depositional ages. We interpret the gap between mineralization age (87Sr/86Sr age) and depositional age of host strata to represent the intrabasinal residence time of sediment storage at the million-year time scale. We also use specimen type to infer relative position of intrabasinal source material along the depositional profile, where oysters represent shallow-water (i.e., proximal) sources and inoceramids represent deeper-water (i.e., distal) sources. The combined use of detrital

strontium isotope ages and specimen types from linked depositional segments provides an opportunity to identify and quantify sediment storage and recycling in ancient source-to-sink systems.
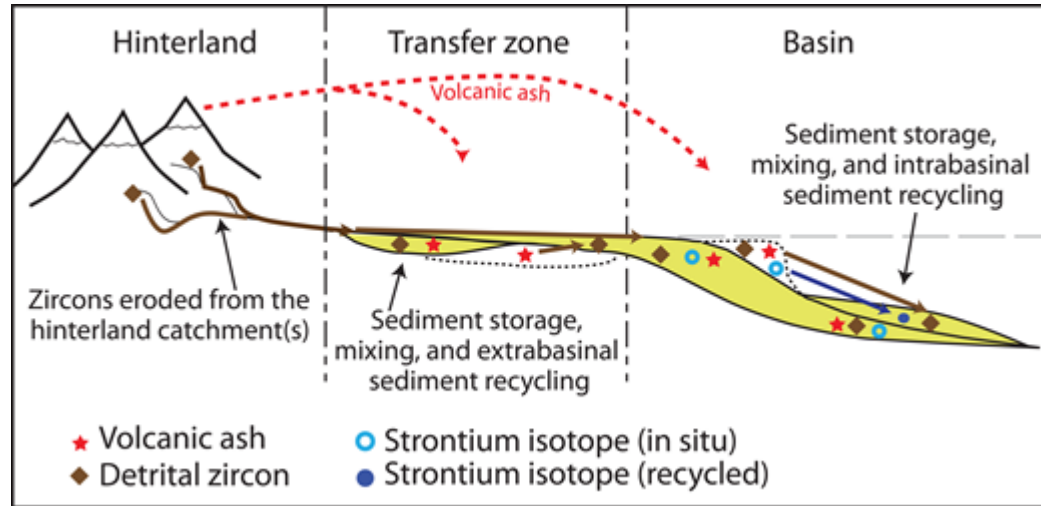

Figure 1. Idealized conceptual cross-section comparing the source, transport, storage, and recycling of detrital grains. Detrital strontium isotopes precipitate, are stored, and subsequently recycled within same basin, providing a record of intrabasinal residence time independent of extrabasinal storage and mixing.
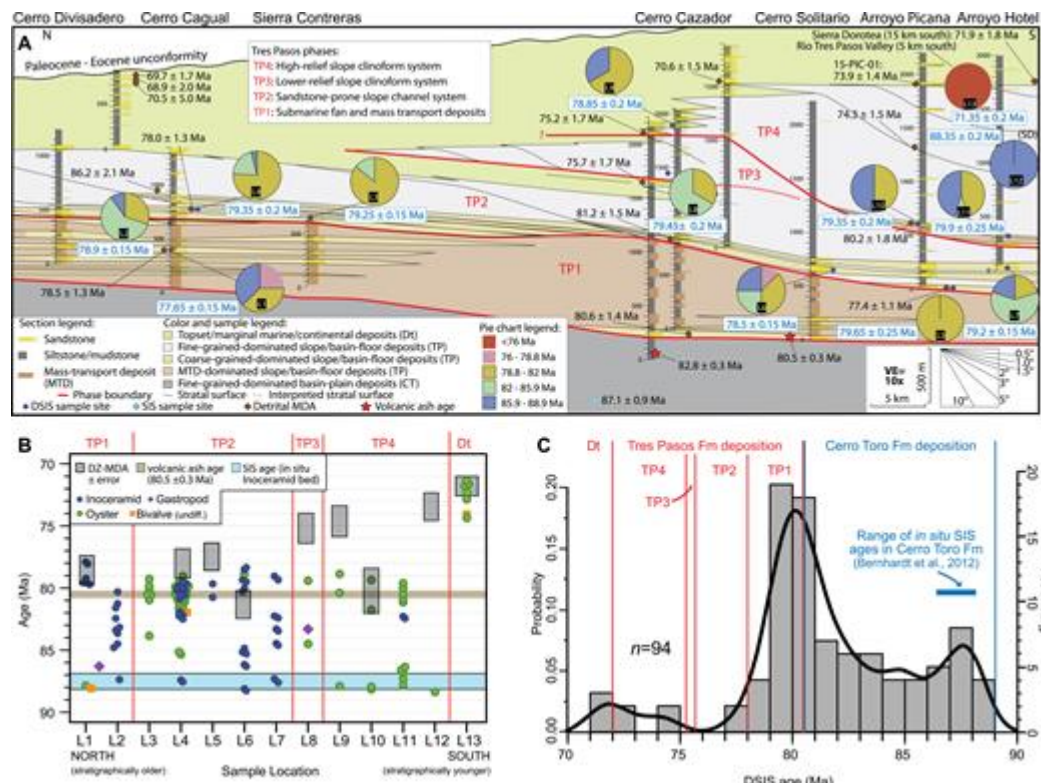

Figure 2. Data and results. (A) Simplified depositional-dip-oriented cross section of the study transect

(modified from Daniels et al., 2018). Pie charts indicate sample age distribution with the youngest detrital strontium isotope stratigraphy (DSIS) age for each location displayed (see Figure 2 for locations). Stratigraphic sections are measured in meters. Stratigraphic units: Dt—Dorotea Formation; TP—Tres Pasos Formation; CT—Cerro Toro Formation. Other abbreviations: SIS—strontium isotope stratigraphy; MDA—maximum depositional age; VE—vertical exaggeration. (B) DSIS ages colored by specimen type and arranged in stratigraphic order (locations L1–L13). DZ-MDA—detrital zircon MDA. (C) Histogram (1 m.y. bins; see the Supplemental Material [see footnote 1]) and kernel density estimate curve for all DSIS ages. Fm—Formation.
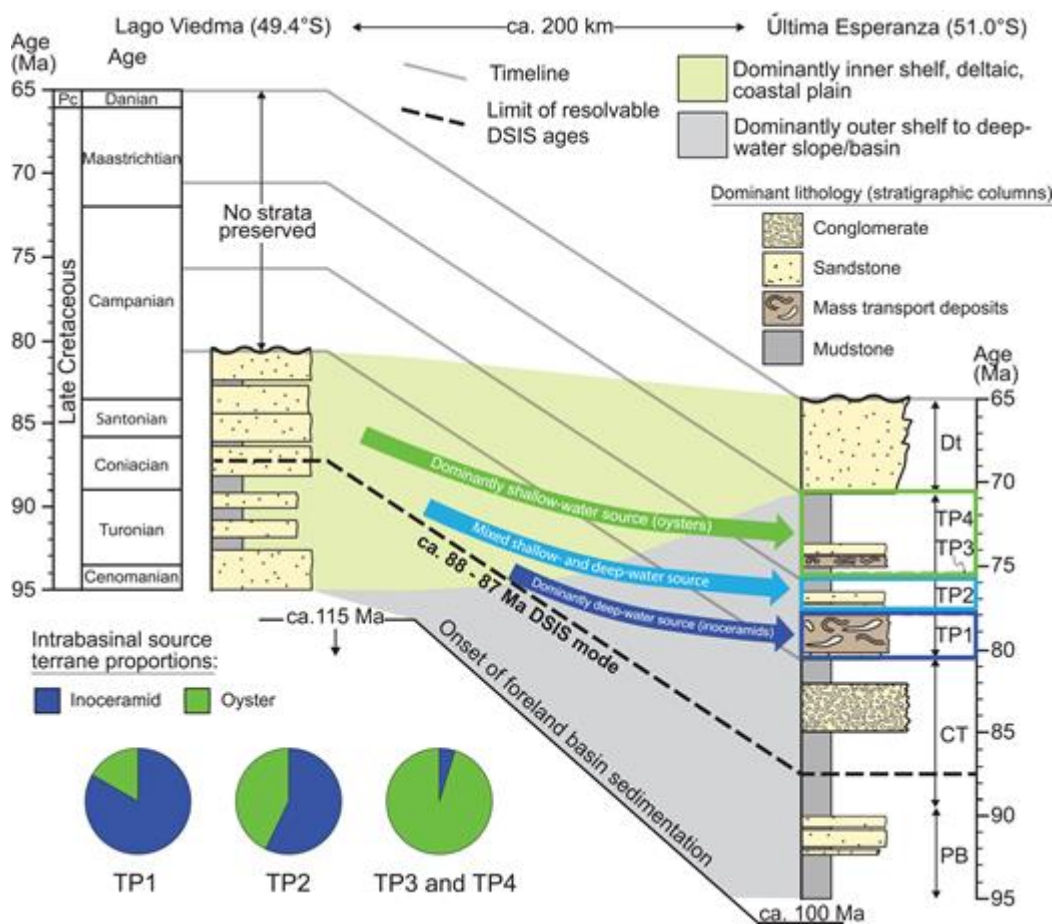

Figure 3. Simplified Magallanes Basin dip profile with Lago Viedma stratigraphy and ages from Malkowski et al. (2017) and Última Esperanza stratigraphy and ages from Daniels et al. (2018). Shaded zones indicate generalized intrabasinal source terranes. Colored arrows and associated boxes indicate the spatiotemporal range and dominant specimen type of intrabasinal recycling recorded in Tres Pasos Formation (TP) strata. Pie charts indicate the proportion of detrital strontium isotope stratigraphy (DSIS) specimen types for each Tres Pasos phase. Pc—Paleocene; Dt—Dorotea Formation; CT—Cerro Toro Formation; PB—Punta Barrosa.
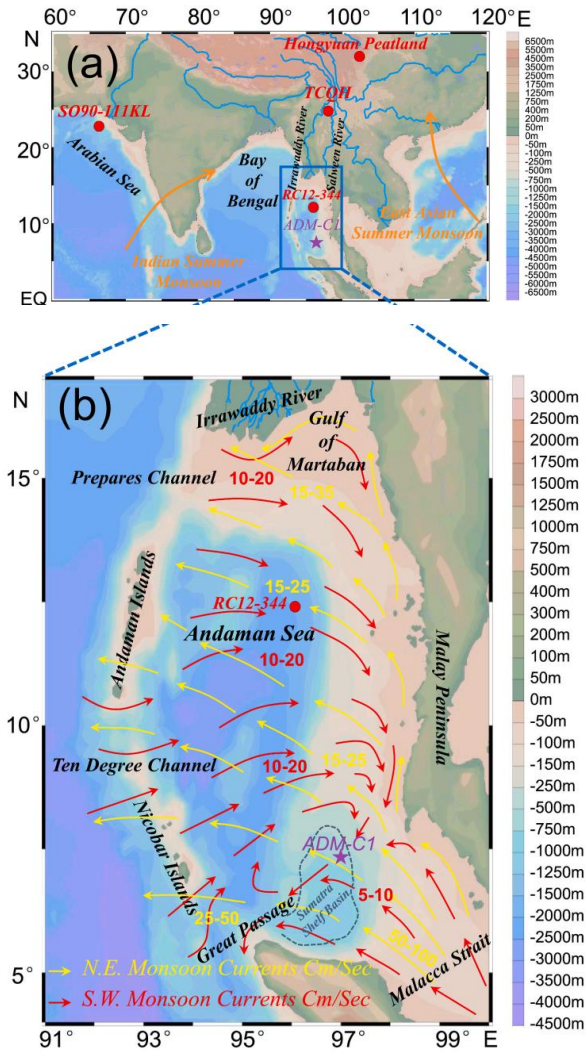
Figure 1. (a) Map of the location of the records referenced in the text. Arrows show the trajectories of the Indian Summer Monsoon and the East Asian Summer Monsoon. Purple star: sediment core ADM-C1 (this study). Red dots: core SO90-111 KL (Schulz et al., 1998), Hongyuan Peatland (Hong et al., 2003), Lake Tengchongqinghai (TCQH) (Zhang et al., 2017a), RC12-344 (Rashid et al., 2007). (b) Monsoon currents in the Andaman Sea. Yellow arrow, northeastern (N.E.) winter monsoon currents; red arrow, southwest (S.W.) summer monsoon currents (modifed from Rodolf, 1969). (For interpretation of the references to colour in this fgure legend, the reader is referred to the Web version of this article.)
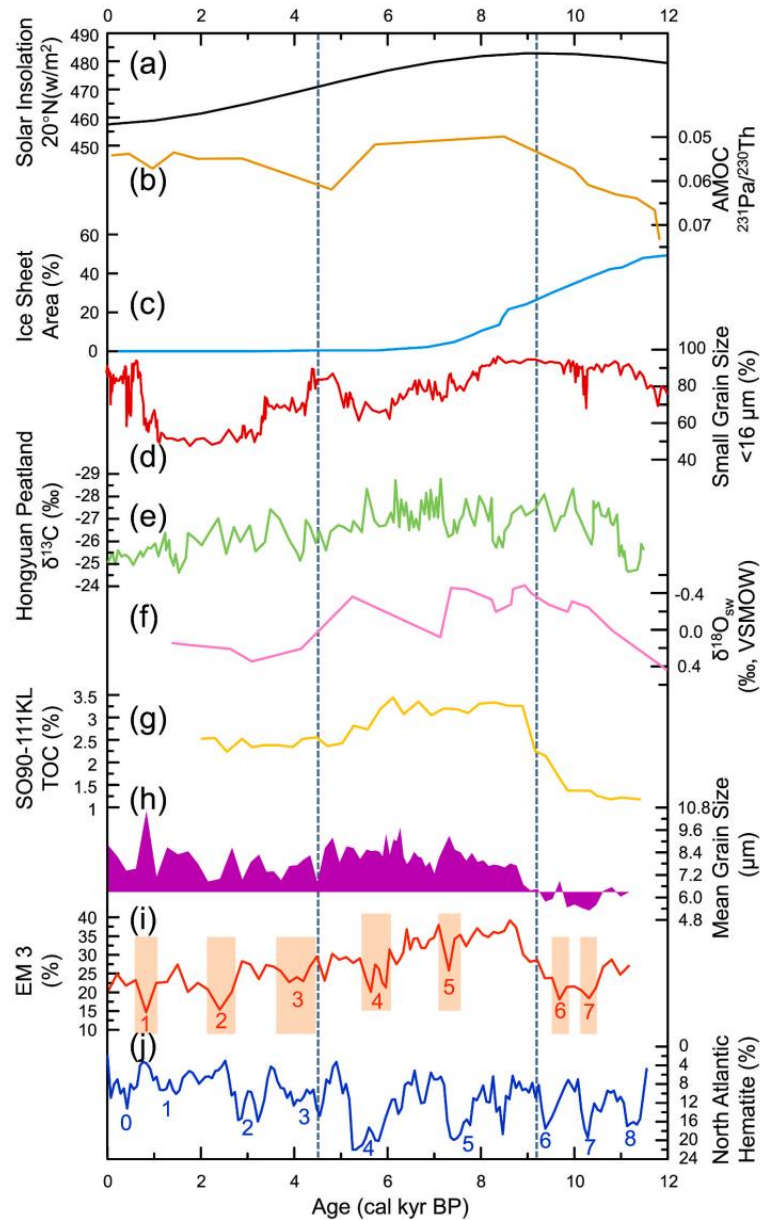
Figure 2. Comparison of Indian Summer Monsoon records. (a) Northern Hemisphere Summer Insolation at 20 °N (Laskar et al., 2004); (b) Sedimentary $^{231}Pa/^{230}Th$ from the North Atlantic (McManus et al., 2004). (c) Percentage area of remnant ice sheets in North America (Dyke, 2004). (d) Small grain-size fraction (<16 μm) in Lake TCQH (Zhang et al., 2017a). (e) $\delta^{13}C$ record of the cellulose of Carex mulieensis from Hongyuan Peatland (Hong et al., 2003). (f) Seawater salinity ($\delta^{18}Osw$) from core RC12-344 (Rashid et al., 2007). (g) Total organic carbon (TOC) content of core SO90-111 KL (Schulz et al., 1998). (h) Mean Grain Size of core ADM-C1. (i) The proportions of EM3. (j) Concentrations of hematite-stained quartz grain in North Atlantic sediments (Bond et al., 2001).